

# **ORIGIN OF TEARING MODE EXCITATION IN THE MST REVERSED FIELD PINCH**

by

**Seung-Ho Choi**

A dissertation submitted in partial fulfillment of

the requirements for the degree of

Doctor of Philosophy

(Electrical Engineering)

at the

**UNIVERSITY OF WISCONSIN-MADISON**

(2006)

UMI Number: 3234612

### INFORMATION TO USERS

The quality of this reproduction is dependent upon the quality of the copy submitted. Broken or indistinct print, colored or poor quality illustrations and photographs, print bleed-through, substandard margins, and improper alignment can adversely affect reproduction.

In the unlikely event that the author did not send a complete manuscript and there are missing pages, these will be noted. Also, if unauthorized copyright material had to be removed, a note will indicate the deletion.

**UMI**<sup>®</sup>

---

UMI Microform 3234612

Copyright 2006 by ProQuest Information and Learning Company.

All rights reserved. This microform edition is protected against unauthorized copying under Title 17, United States Code.

ProQuest Information and Learning Company  
300 North Zeeb Road  
P.O. Box 1346  
Ann Arbor, MI 48106-1346

# A dissertation entitled

ORIGIN OF TEARING MODE EXCITATION IN THE  
MST REVERSED FIELD PINCH

submitted to the Graduate School of the  
University of Wisconsin-Madison  
in partial fulfillment of the requirements for the  
degree of Doctor of Philosophy

by


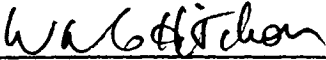


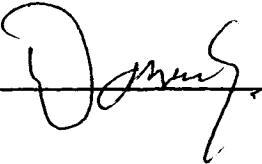

SEUNG\_HO CHOI

**Date of Final Oral Examination:**

Month & Year Degree to be awarded: **December** JUNE<sub>9</sub> 2006 **May** **August** 2006

\*\*\*\*\*

### Approval Signatures of Dissertation Committee

Signature, Dean of Graduate School



# Origin of tearing mode excitation in the MST

## Reversed Field Pinch

Seung-Ho Choi

Under the supervision of Professor Stewart C. Prager and Dr. Darren Craig  
at the University of Wisconsin-Madison

In this thesis we investigate the origin and coupling between different modes, focusing primarily on modes resonant near the edge of the plasma. We investigate mode stability by direct measurement of the terms in MHD which represent the energy flow between the modes and the equilibrium field. We also examine the nonlinear coupling between modes with bi-spectral techniques. This information could be useful in efforts to reduce the dominant fluctuations and improve the fusion energy potential of the RFP. These studies also yield new insight into the origin of reconnection in these plasmas. The cause for reconnection mode growth is determined experimentally for three cases: standard RFP sawtooth crash, enhanced confinement (EC)  $m=0$  bursts, and slow growth quasi-single helicity (QSH). We measure the term in MHD equations which represents the driving (or damping) of tearing modes due to the equilibrium magnetic field. With sawtooth crash, the term is negative for modes with  $m=0$ , indicating that energy flows from the mode to the axisymmetric fields. A significant measured bi-spectrum between the  $m=0$  and  $m=1$  modes indicates that nonlinear coupling is present. This supports the standard picture that  $m=0$  modes are stable, but  $m=0$  reconnection is driven by nonlinear coupling to other modes. In the EC  $m=0$  bursts, an opposite picture holds:  $m=0$  modes

derive energy from the axisymmetric fields indicating they are unstable, corresponding to spontaneous reconnection. Such a picture awaits theoretical study and more complete equilibrium profile measurements. In the slow growth QSH plasmas, the term for the  $m=1$  mode in the poloidal component is very weak and mostly negative and for the toroidal component is strong and mostly positive. Because of the large noise, we cannot determine with certainty the sign of the linear term for either component and the result for the QSH case is inconclusive. These results support the possibility that nonlinear mode coupling could be important in reconnection in other laboratory and astrophysical venues. These techniques might also be useful to examine and understand how these modes are produced and may lead to improved ways to control them.

## Acknowledgement

I really appreciate to my God so much for guiding my life. I want to say “Glory to God”. I am so glad that I have two kind and intelligent advisors who provide me the best assistance to pursuit the Ph.D. degree. Great appreciation should go to my both advisors, Professor Stewart Prager and Dr. Darren Craig, who have been so patient and inspiring in physics research. I also would like to appreciate to my prelim and thesis committee member, Dr. David Anderson, William Hitchon, Carry Forest, Chris Hegna, and Carl Sovinec, for the useful and inspiring discussions during presentation.

For countless experimental insight, diagnostic support, and useful discussion, thanks should go to many scientists. These include John Sarff, Abdul Almagri, Gennady Fiksel, and Jay Anderson. I would like to thank Abdul Almagri for helping me to make the b-dot probe.

I have to thank to my parents, Sang Choi and Young Kim, who have been so helpful and supporting to me in pursuing the advanced educational degree. I also have to say thank-you to my wife, Sunju Choi and her parents, Byung Yoon and Soon Park.

# Contents

1	Introduction	
1.1	Reversed Field Pinch.....	1
1.2	Dominant mode in the RFP.....	3
1.3	Behavior of $m=0$ and $m=1$ modes in sawtooth, EC, and QSH plasmas.....	4
1.4	Measurement approach.....	8
1.5	Outline and overview.....	9
2	Diagnostics	
2.1	Introduction.....	11
2.2	Magnetic coil array.....	12
2.3	Movable b-dot probe.....	16
2.4	Movable triple Langmuir probe.....	20
3	Analysis Method	
3.1	Identification of poloidal and toroidal mode numbers at the boundary....	24
3.2	Ensemble average.....	26
3.3	Identification of modes from one point internal measurements.....	27
3.4	Bi-spectrum.....	31

<b>4</b>	<b>Measurement of individual equilibrium and fluctuation quantities</b>	
4.1	Introduction.....	38
4.2	Three different plasmas-sawtooth, EC, QSH.....	38
4.3	Measurements of equilibrium quantities.....	40
4.4	Measurements of fluctuation quantities.....	46
<b>5</b>	<b>Linear and nonlinear stability in <math>m=0</math> and <math>m=1</math> modes</b>	
5.1	Introduction.....	56
5.2	Linear stability of $m=0$ mode in the sawtooth.....	57
5.3	Comparison with MHD computation.....	59
5.4	Nonlinear stability of $m=0$ mode in sawtooth.....	60
5.5	Linear stability of $m=0$ mode in EC.....	63
5.6	Linear stability of $m=1$ mode in QSH.....	66
5.7	Summary.....	68
	Appendix.....	70



## 1 INTRODUCTION

Reversed field pinch (RFP) plasmas are characterized by many fluctuations in the magnetic field due to the weak magnetic field used to confine the plasma. These fluctuations are connected with reconnection of magnetic fields inside plasma and affect much of the macroscopic dynamics in the RFP. The fluctuations can be decomposed into Fourier modes and only a few modes are dominant in the RFP. The origin of these dominant modes has been studied for many years but open questions remain. In this thesis we investigate the origin and coupling between different modes, focusing primarily on modes resonant near the edge of the plasma. We investigate mode stability by direct measurement of the terms in MHD which represent the energy flow between the modes and the equilibrium field. We say the mode is stable if the mode loses energy to the equilibrium field. We say the mode is unstable if the mode gains energy from the equilibrium field. We also examine the nonlinear coupling between modes with bi-spectral techniques. This information could be useful in efforts to reduce the dominant fluctuations and improve the fusion energy potential of the RFP. These studies also yield new insight into the origin of reconnection in these plasmas.

### 1.1 Reversed Field Pinch (RFP)

The reversed field pinch (RFP) is an axisymmetric, toroidal magnetic configuration. The RFP is an excellent candidate for the core of a compact, economical fusion reactor. The Madison Symmetric Torus (MST) is a toroidal reversed field pinch device with a minor radius of  $a=0.52\text{m}$  and a major radius of  $R=1.5\text{m}$  used for plasma physics and fusion research (Fig. 1.1).

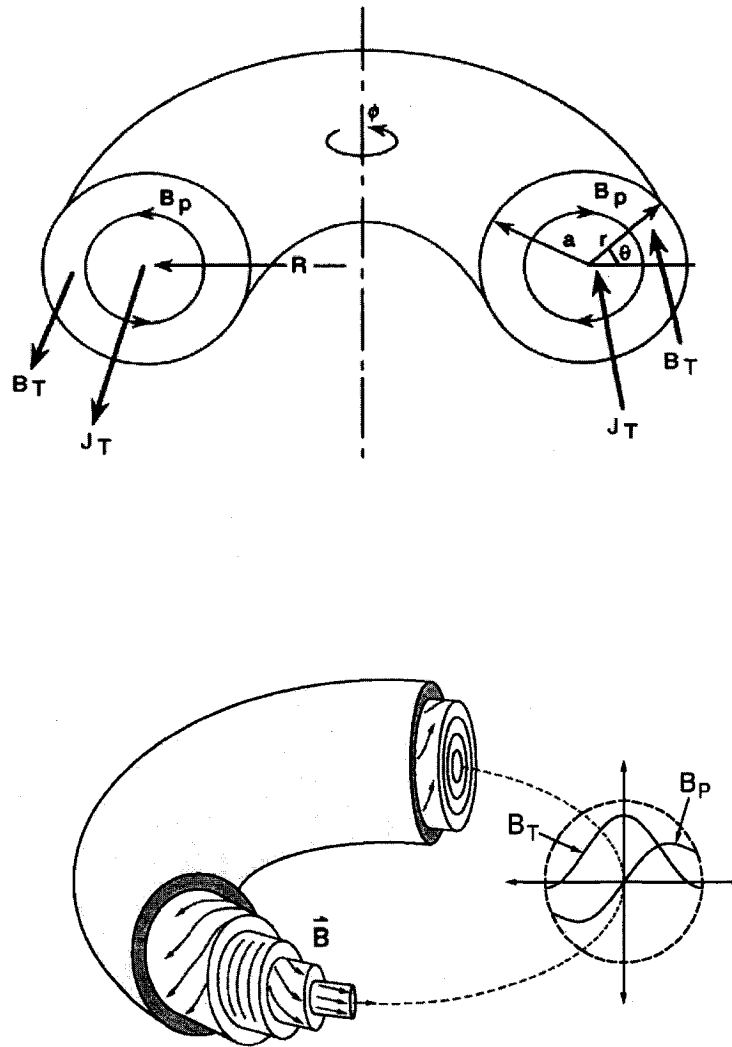


Figure 1.1 Reversed field pinch configuration

The plasma is confined by both a toroidal magnetic field ( $B_T$  or  $B_\phi$ ) and a poloidal magnetic field ( $B_p$  or  $B_\theta$ ) and the toroidal magnetic field is reversed at the edge of the plasma (Fig. 1.1). The poloidal magnetic field is produced by the toroidal current density ( $J_T$ ) (Fig. 1.1). In figure 1.1,  $\phi$  is the toroidal angle and  $\theta$  is the poloidal angle. Like the

tokamak, the RFP is a toroidal, magnetically confined plasma system, but the applied toroidal field strength is about ten times smaller.

## 1.2 Dominant modes in the RFP

The presence of even a small resistivity allows the magnetic field lines to reconnect resulting in a change in magnetic topology. Tearing modes [1,2], so named because the magnetic field “tears” and reconnects at singular surfaces, are the dominant instabilities in the RFP. Singular surfaces are toroidal surface where the mode wave number parallel to the equilibrium magnetic field vanishes and are called singular because the MHD differential equation for the mode evolution is singular there. Many tearing modes are observed in experiment. Figure 1.2 shows the safety factor profile for an MST plasma. The safety factor is defined as  $q = \frac{rB_\phi}{RB_\theta}$  and the singular surfaces for

several modes, where  $q = -\frac{m}{n}$ , are labeled.

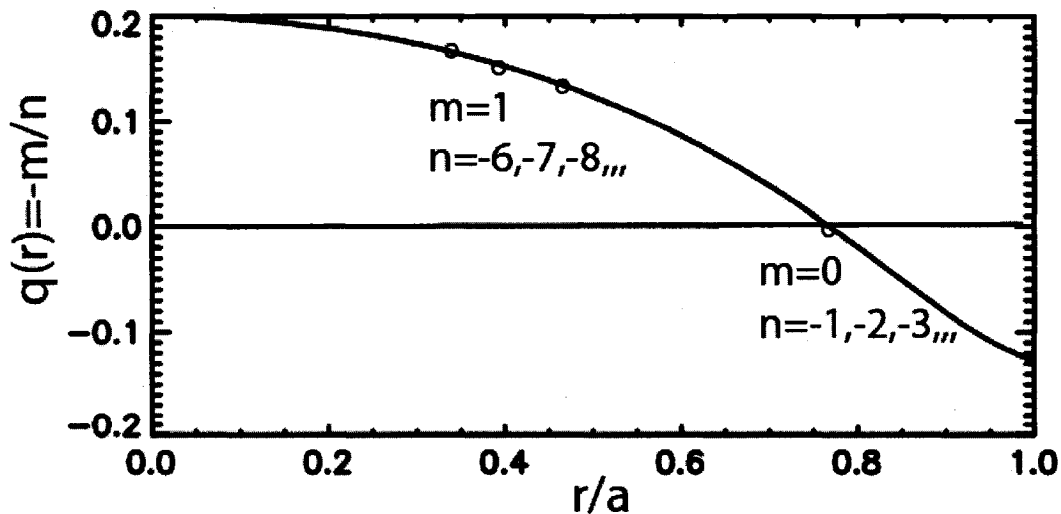


Figure 1.2 Safety factor profile in RFP and location of singular surfaces for several modes

The  $m=0$  modes are called edge modes and the  $m=1$  modes are called core modes because of the location of their singular surfaces (or resonant surfaces). The tearing modes are very important for RFP dynamics. These modes produce MHD dynamo [3,4] and affect transport [5]. The temporal behavior of the  $m=0, 1$  modes differs for different plasmas. In the next section, we describe 3 particular types of mode excitation that will be examined in this thesis.

### 1.3 Behavior of $m=0$ and $m=1$ modes in sawteeth, EC, and QSH plasmas.

Three kinds of plasmas are examined in this thesis: normal RFP plasmas (sawteeth), Enhanced confinement (EC) plasmas, and Quasi-single helicity (QSH) plasmas.

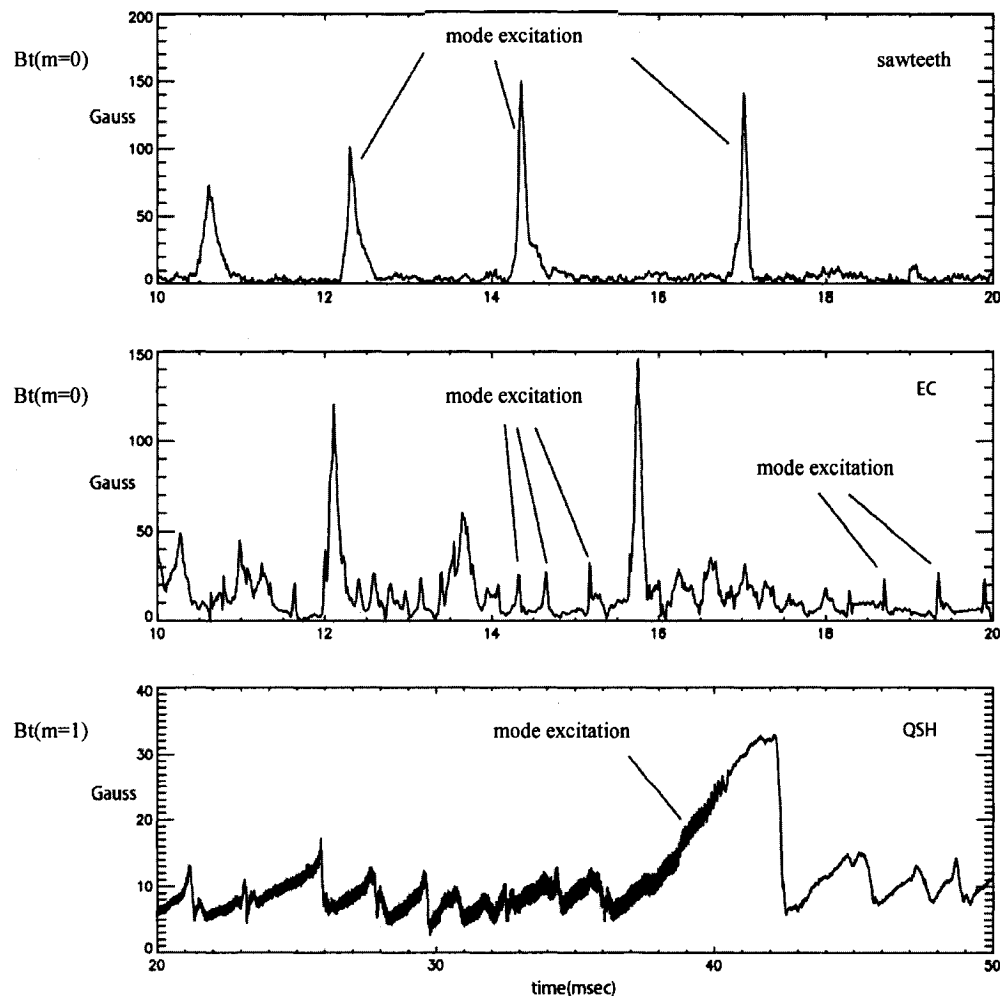


Figure 1.3  $m=0,1$  modes vs time, showing time periods of mode excitation examined in this thesis

Figure 1.3 shows the  $m=0, 1$  modes during a typical shot for each plasma type. In each case, one or more tearing modes are excited and grow in time. In this thesis we investigate the cause of this growth which corresponds to reconnection at the singular surfaces.

The sawtooth, in which the magnetic flux is self-generated, is a common feature of standard RFP plasmas (Fig. 1.4). The sawteeth are superimposed on a slow time evolution of the total toroidal magnetic flux (or volume averaged toroidal magnetic field) that is largely determined by the Madison Symmetric Torus (MST) external circuit. The flux rises with the plasma current during the initial portion of the discharge and enters the flat-top region of the shot before decaying and terminating (Fig. 1.4).

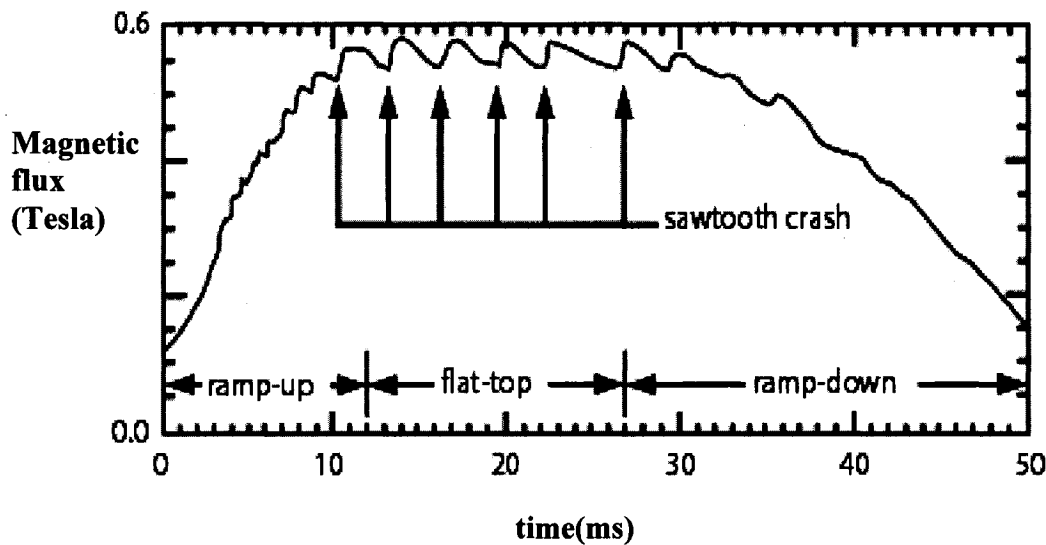


Figure 1.4 Volume averaged toroidal magnetic flux in whole shot

The sawtooth oscillation represents a discrete manifestation of the dynamo which maintains the reversed configuration in the MST. During the sawtooth crash, the volume averaged toroidal magnetic field rapidly jumps by around 5~10% of its mean value and modes with poloidal mode number  $m=0$  and 1 are strongly excited. The sawtooth crashes are global events affecting all observable quantities (electron density, temperature,

magnetic field etc.) in a reproducible fashion. The reproducible fashion means that we can make a large ensemble [3] of the sawtooth crashes. This is a key capability of MST, important for the analysis in this thesis. As an example, we can characterize the current profile flattening at a sawtooth crash with the alpha parameter, related to the parallel current by the following equation:

$$\frac{\mu_0 J_{\parallel}}{B} = \lambda_0 \left(1 - \left(\frac{r}{a}\right)^{\alpha}\right).$$

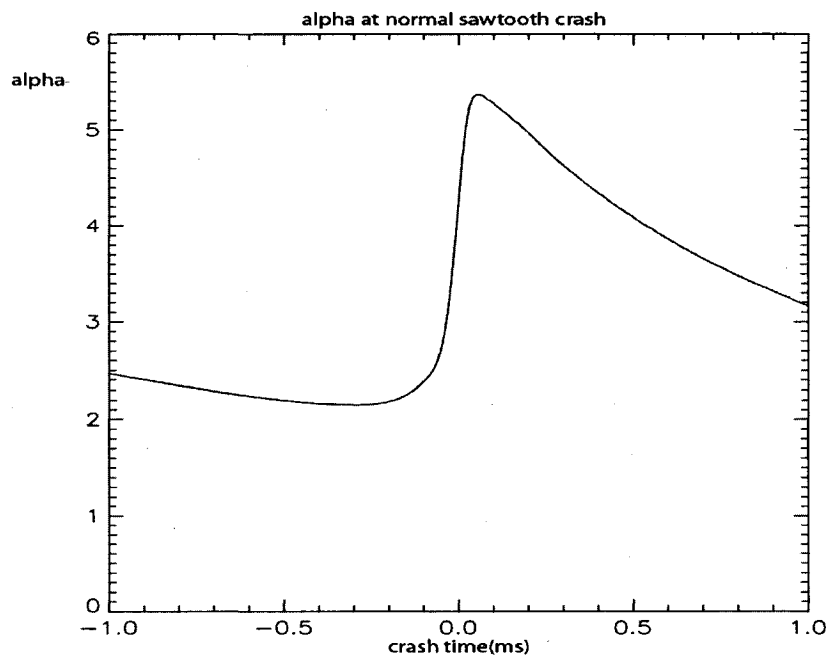


Figure 1.5 Alpha ( $\alpha$ ) parameter is jump up at sawtooth crash

Figure 1.5 shows an average of  $\alpha$  over 1000 sawtooth crashes and one can see that the current profile broadens and the system moves closer to the Taylor relaxed state [7] with flat current profile.

The sawtooth cycle in the RFP has been studied for many years in MHD computation [6]. A prediction of this work is that the  $m=0$  growth at a sawtooth crash is not due to linear instability, but rather is the result of the nonlinear coupling of core

resonant  $m=1$  modes. Figure 1.6 (a) shows the sawtooth cycle average behavior of both  $m=0$  and  $m=1$  modes and clearly both are excited together, consistent with the idea that nonlinear coupling may be the cause for  $m=0$  growth. In this thesis, we test this idea experimentally and find that indeed the  $m=0$  modes are stable throughout the crash and that the  $m=0$  and  $m=1$  modes exhibit strong nonlinear coupling.

EC plasmas are relatively newer and have not been studied in computation. In EC plasmas, the confinement spontaneously improves and the sawtooth cycle time is extended [9]. Between normal sawteeth smaller bursts in  $m=0$  modes are observed (Fig. 1.3). The EC bursts of  $m=0$  modes are not accompanied by bursts in the core resonant  $m=1$  modes as shown in figure 1.6 (b). Similar  $m=0$  bursts are observed in PPCD plasmas [8]. We focus our attention in this thesis on the spontaneous enhanced confinement obtained at very deep reversal and low density. The origin of these bursts is unknown but there is speculation that they are due to changes in the edge profiles of current or pressure and subsequent linear instability[9]. We find experimentally that the  $m=0$  modes are unstable during these bursts, in contrast to the sawtooth crash in normal RFP plasmas.

A third case of mode excitation recently observed in experiment is the quasi-single helicity (QSH) plasma [10]. In QSH, one  $m=1$  mode becomes dominant and grows very slowly (Fig. 1.3). We examine QSH plasmas in which the edge  $q=0$ . Therefore, the edge mode ( $m=0$ ) is resonant just near the conducting shell of MST and is strongly suppressed. (QSH can also be obtained in fully reversed plasmas but we do not consider these here.) Figure 1.6 (c) shows the average behavior of the  $m=1$ ,  $n=5$  during QSH with slow steady mode growth. The core resonant  $m=1$  modes are expected to be slightly unstable or marginally stable. We explore this possibility experimentally in this thesis.

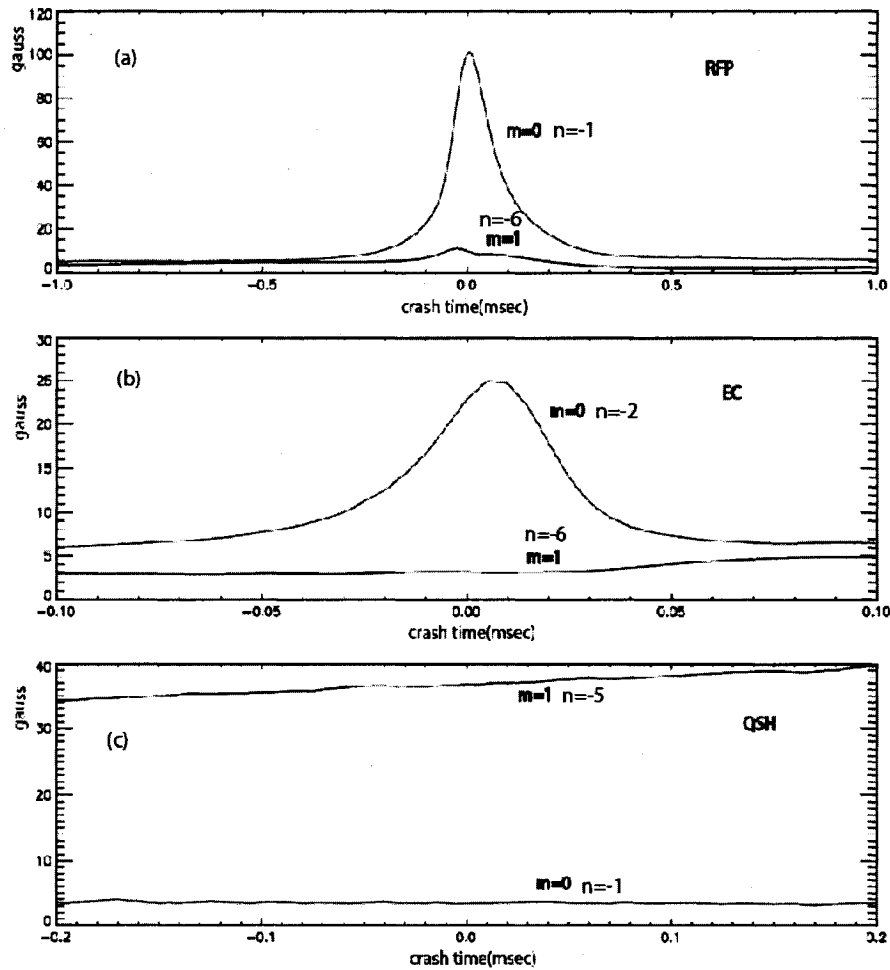


Figure 1.6 Ensemble averaged magnitude of typical  $m=0$  and  $m=1$  modes in each plasma

#### 1.4 Measurement approach

To explore the cause of mode growth in each case, we use the novel approach of directly measuring terms in the MHD equation for the mode energy evolution. The MHD energy drive terms can give the information about how the energy flows between the modes and equilibrium fields and between different modes. For example, the equation for  $m=0$ ,  $n=-1$  mode evolution in MHD is:



$$\frac{\partial \vec{b}_{0,-1}}{\partial t} = \nabla \times (\vec{v}_{0,-1} \times \vec{b}_{0,0}) + \nabla \times (\vec{v}_{0,0} \times \vec{b}_{0,-1}) + \sum_{\substack{0=l+m \\ -1=p+q}} \nabla \times (\vec{v}_{l,p} \times \vec{b}_{m,q}) + \frac{\eta}{\mu_0} \nabla^2 \vec{b}_{0,-1}$$

The first two terms on the RHS represent energy exchange between the mode and axisymmetric fields. The summation represents nonlinear interaction between modes. The last term represents resistive dissipation. The second and last terms are measured with probes to be small relative to the first term. The sign of each drive term in the MHD equation gives important information about stability. If the first term in the RHS is negative, it means the mode is losing energy to the equilibrium fields. Hence the mode is stable. If it is positive, it means the mode is gaining energy from the equilibrium fields. Hence the mode is unstable. We will assume that the sign of the linear term is independent of radius.

## 1.5 Outline and overview

This thesis is divided into 5 chapters and an appendix. In Chapter 2, diagnostic methods for magnetic field and electrostatic potential (used to infer MHD velocity) are discussed. The method for determining mode numbers  $m$  and  $n$  from probe data and the ensemble average method used to approximate a poloidal and toroidal average are explained in Chapter 3. The bi-spectrum is also described in Chapter 3. The experimental application of the bi-spectrum shows that there is a strong nonlinear coupling between  $m=0$  and  $m=1$  modes at the edge of MST. The fluctuation measurements used to evaluate terms in the MHD equations are presented in Chapter 4. The MHD velocity is determined from the Langmuir probe floating potential measurement assuming the velocity is equal to the  $E \times B$  velocity. In Chapter 5, the fluctuation data are combined to form the terms in the MHD equations for mode evolution. This is done for three kinds of mode

excitation; sawtooth crash, EC  $m=0$  burst, and QSH. The  $m=0$ ,  $n=-1$  mode is shown to be stable during a normal sawtooth crash. The presence of large bi-spectrum between  $m=0$  and  $m=1$  modes during the crash strongly implies that the energy source for the  $m=0$  is nonlinear coupling to  $m=1$  modes. The  $m=0$ ,  $n=-2$  mode is shown to be unstable during the EC burst. This is consistent with the observed absence of  $m=1$  mode excitation during the EC burst. The  $m=1$ ,  $n=-5$  mode in QSH is examined but the stability measurement is inconclusive. The slow mode growth in QSH and the fact that the velocity fluctuations at the edge are not well resolved result in a large error. The error analysis in various order correlation functions is explained in the appendix.

### References

1. P.H. Rutherford, *The Physics of Fluids* **16**, 11 (1973)
2. H.P. Furth *et al.*, *The Physics of Fluids* **16**, 7 (1973)
3. J.T. Chapman, Ph.D thesis, University of Wisconsin, Madison, 1998
4. P.W. Fontana *et al.*, *Phys. Rev. Lett* **85**, 3 (2000)
5. M.S. Stoneking *et al.*, *Phys. Rev. Lett* **73**, 4 (1994)
6. Y. L. Ho, G. G. Craddock, *Physics of Fluids B* vol 3 pp721-734 (1990)
7. J.B. Taylor *et al.*, *Phys. Rev. Lett* **33**, 139 (1974)
8. J.S. Sarff, S.A. Hokin, H. Ji, S.C. Prager, and C.R. Sovinec, *Phys. Rev. Lett* **72**, 3670 (1994)
9. B.E. Chapman, C.S. Chiang, S.C. Prager, J.S. Sarff, and M.R. Stoneking, *Phys. Rev. Lett.* **80**, 2137 (1998)
10. P. Martin *et al.*, *Nuclear Fusion* **43**, 1855 (2003)

## 2 Diagnostics

### 2.1 Introduction

To measure the mode driving terms in the MHD equation we must measure the fluctuating magnetic field and velocity (deduced from the measured electric field). The magnetic and electric fields are measured with a variety of probes. Magnetic sensors are commonly used to measure the magnetic properties of plasma experiments. Probes consist of copper wire coils encased in a non-conducting heat shield and one or more layers of conducting material such as graphite, stainless steel or a thin layer of silver paint as an electrostatic shield. Magnetic sensors are used both inside and outside of the plasma to measure the equilibrium and fluctuating field in MST. For measurement of the linear term in the MHD equation, two kinds of magnetic sensor probes are used. One is the movable magnetic coil probe for measurement of the magnetic field inside MST. The other is the magnetic coil array located at the edge of MST to measure the magnetic fluctuation spectrum. These coils must be calibrated for useful measurements.

We also measure the electric field in the plasma to deduce the  $E \times B$  velocity.

The electric field fluctuation,  $\vec{E} = -\vec{\nabla}\tilde{\phi}_p - \frac{\partial\vec{A}}{\partial t}$ , is dominantly electrostatic ( $\vec{\nabla}\tilde{\phi} \gg \frac{\partial\vec{A}}{\partial t}$ ).

We measure the electrostatic potential with a triple Langmuir probe using the relation,  $\phi_p = \phi_f + \alpha T_e$ , where  $\phi_p$  is the plasma potential,  $\phi_f$  is the floating potential, and  $T_e$  is the electron temperature [1,2]. We use  $\alpha = 2.2$  for MST corrections. The value of  $\alpha$  in MST have been studied and derived in many past theses in MST group. The parallel component (to magnetic field) of velocity is not needed in the MHD equation for mode energy evolution because the  $v \times B$  term is the important term.

Measurements at two different radial points are needed to find the radial derivative for the electric field. Below we describe the edge magnetic coil array and its calibration (section 2.2), the movable B-dot probe and its calibration (section 2.3) and the Langmuir probe (section 2.4).

## 2.2 Magnetic coil array

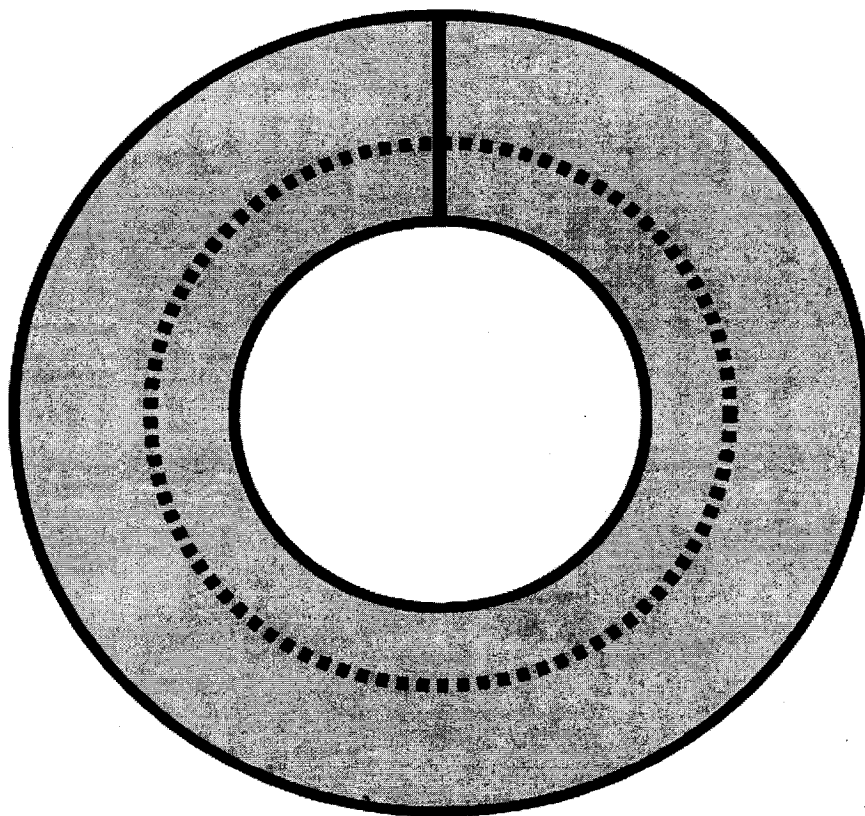


Figure 2.1 Top view of MST showing the location of edge toroidal array of magnetic coils

An array of 64 magnetic coil triplets is mounted on the inner surface of the vacuum vessel. Each coil set consists of three orthogonal magnetic sensors, oriented to measure the magnetic field in poloidal, toroidal and radial directions. The radial component of the magnetic field is very small at the edge of MST because the wall of

MST is a conductor. These encapsulated coil forms are mounted on the inside of MST as shown in figure 2.1. The electrostatic and heat deposition shield is a graphite box. The large coherent structure of the dominant magnetic modes allows edge coils to be used to characterize magnetic fluctuations throughout the plasma. Because these coils do not interfere with the plasma, edge fluctuating magnetic field measurements may be made at multiple positions and then correlated to derive information about the spatial structure of the modes. One common technique employs coil arrays to sample the magnetic perturbation at regularly spaced intervals enabling Fourier decomposition of the measured fluctuations. We employ the toroidal array of 64 coil sets evenly distributed in toroidal angle and at a poloidal angle of 241 degrees (relative to the outbound midplane). These 64 coil sets can provide the resolution of the toroidal or poloidal magnetic field fluctuations up to  $n=32$  ( $n$  is toroidal mode number). Since the coils are all at the same poloidal angle ( $241^\circ$ ), the decomposition into different  $m$  number (poloidal mode number) is impossible. We can write the magnetic field at  $241^\circ$  as

$$B(\phi_i) = \sum_{n=0}^{N/2} a_n \sin(n\phi_i) + b_n \cos(n\phi_i) = \sum_{n=0}^{N/2} c_n \cos(n\phi_i - \delta_n) \quad (2.2)$$

$$(\phi_i - \phi_{i-1}) = \Delta\phi = \frac{2\pi}{N}$$

where  $B(\phi_i)$  denotes the poloidal or the toroidal magnetic field measured by the coils and  $N$  is the number of coils in use. The toroidal angle  $\phi_i$  has discrete values according to the number ( $N$ ) of coils in use. The relations between  $a$ ,  $b$ ,  $c$ , and  $\delta$  are

$$\begin{aligned} a_n &= c_n \sin(\delta_n) \\ b_n &= c_n \cos(\delta_n) \end{aligned} \quad (2.3)$$

The  $N$  coil measurements and  $N/2$  modes give  $N$  equations with  $N$  unknowns  $(a_1, a_2, \dots, a_{N/2-1}, b_0, b_1, b_2, \dots, b_{N/2})$ , where two unknowns  $a_0$  and  $a_{N/2}$  disappear

because the sine term in the equation 2.2 is zero for  $n=0$  and  $N/2$  due to  $\Delta\phi = \frac{2\pi}{N}$ .

Therefore we have the resolution up to  $n=N/2$  when we use  $N$  coil sets.

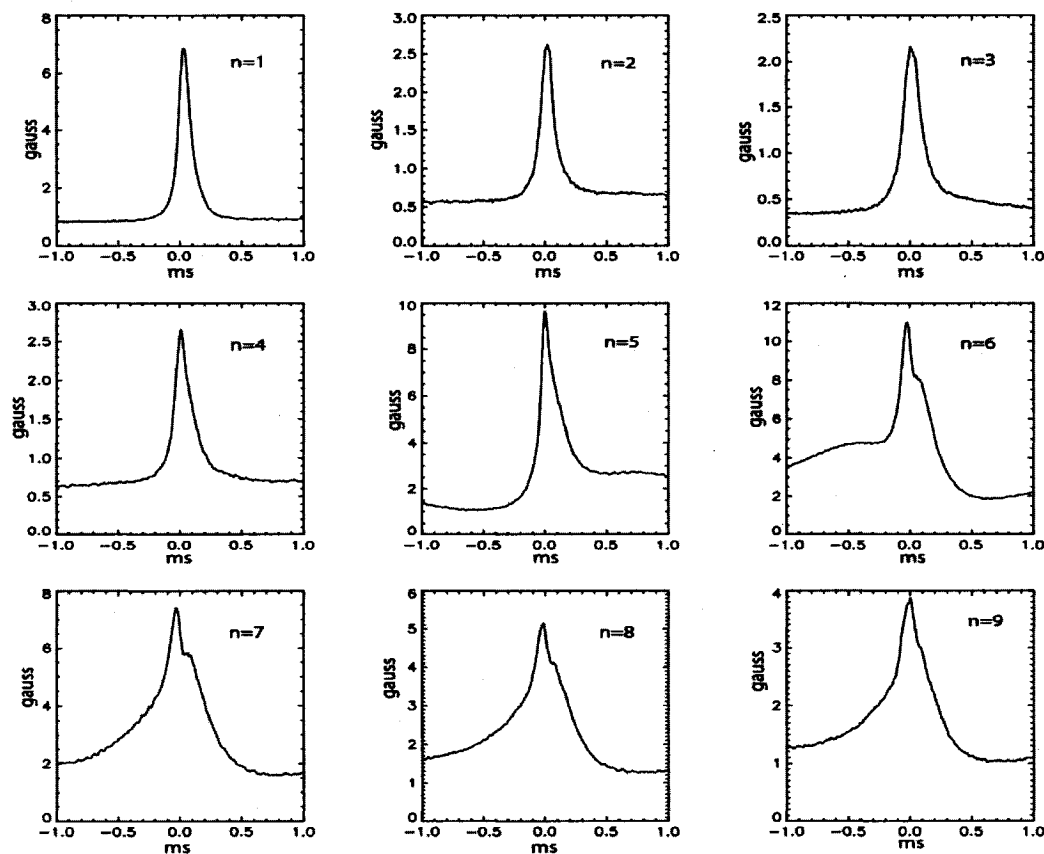


Figure 2.2 Magnitude of toroidal modes of  $B_p$  from edge magnetic coils, the time  $t=0$  marks the time of the sawtooth crash.

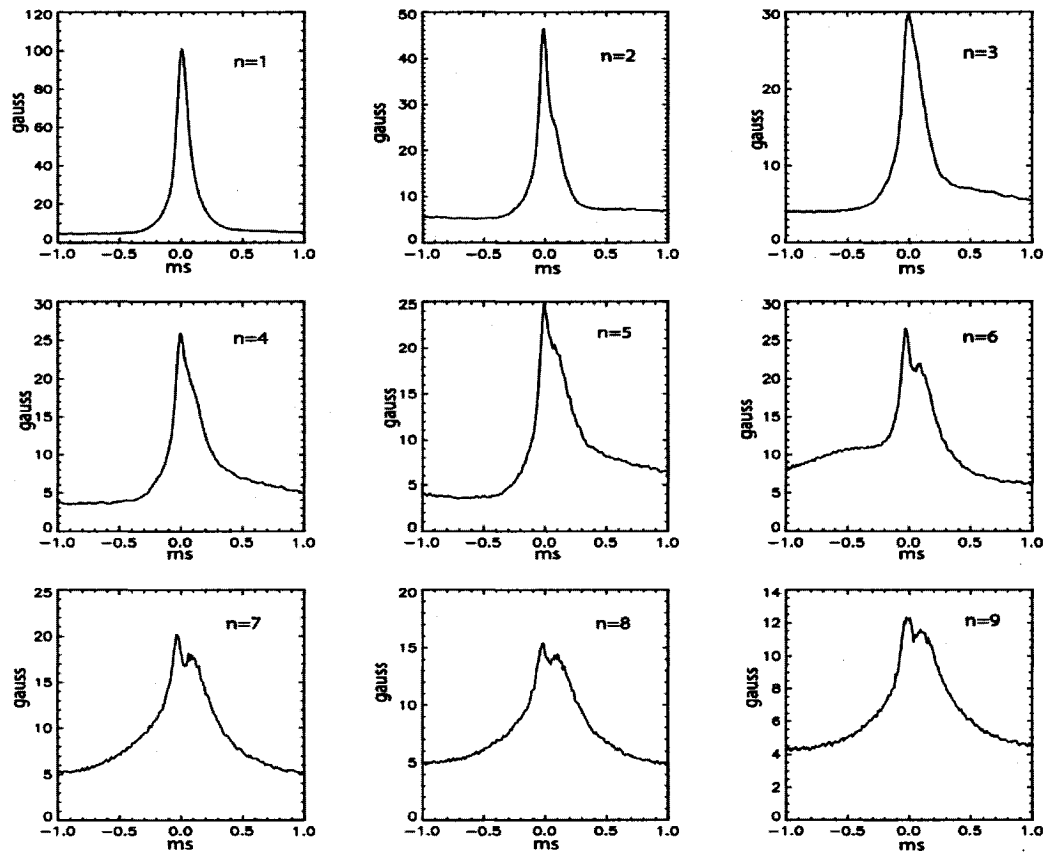


Figure 2.3 Magnitude of toroidal modes of Bt from edge magnetic coils, the time  $t=0$  marks the time of the sawtooth crash.

Figure 2.2 shows the magnitudes of poloidal magnetic fields with toroidal mode numbers  $n=-1\sim-9$  and they are all excited at the burst time  $t=0$ . Figure shows time period before 1 ms and after 1 ms of burst time  $t=0$ . The y-scale in figure 2.2 is larger for  $n=-5$  and above. This is because the modes with  $n=-5,-6,-7\dots$  are resonant modes and they have  $m=1$  to satisfy the resonance condition  $q=-m/n$  (Fig 1.6). Figure 2.3 shows the magnitude of toroidal magnetic fields with toroidal mode number  $n=-1\sim-9$  and they are all excited at the burst time  $t=0$  as same as in the figure 2.2. The magnitude of the  $n=-1$  mode is the biggest and the mode amplitude decreases with  $n$  number. The modes with  $n=-1,-2,-3,-4$  are resonant modes and have  $m=0$ . The  $n=-5,-6,-7\dots$  are a mixture of  $m=0$  and  $m=1$ . This

can be established by using the fact that the radial current density nearly vanishes at the wall and is explained clearly in chapter 3. Table 2.1 summarizes the relative size of the different components for the resonant modes of interest.

<b>Resonant modes</b> <b><math>q=-m/n</math></b>	<b>Bt (toroidal magnetic field)</b>	<b>Bp (poloidal magnetic field)</b>
$m=0$ $n=-1,-2,-3,-4,-5,-6,\dots$	Large and decreasing as $n$ gets larger	Very small in any $n$ number
$m=1$ $n=-5,-6,-7,-8,\dots$	Moderate and decreasing as $n$ gets larger	Moderate and decreasing as $n$ gets larger

Table 2.1 Magnitude of toroidal and poloidal magnetic field according to resonant mode number

The magnetic coil array needs the calibration for more reliable measurements. The coil alignments are not known precisely. Imperfect alignments cause coils, designed to measure Bt (toroidal magnetic field) or Bp (poloidal magnetic field) signal only, to measure  $k*Bt + s*Bp$  instead. Each coil really has sensitivity to both Bp and Bt fields ( $s$  and  $k$  here). Once the above sensitivity ( $s$  and  $k$ ) is taken into account, the Bt and the Bp signals are converted to Gauss using an effective coil area of  $1.5\text{ cm}^2$  taken from calibrations [4] before mounting inside the MST.

### 2.3 Movable b-dot probe

The movable b-dot probe [5] is used for measuring the magnetic fluctuations inside the plasma near the wall. The probe in our experiment has two displaced sets of



coils (toroidal, poloidal, and radial). Two sets of coils are located at different radial points near the wall. The number of turns are optimized for the size and the shape of the B-dot probe resulting in 20 to 30 turns for each coil. The set of all coils is boron nitride shielded. Electrostatic shield is provided by silver painting inside the wall of the boron nitride shield.

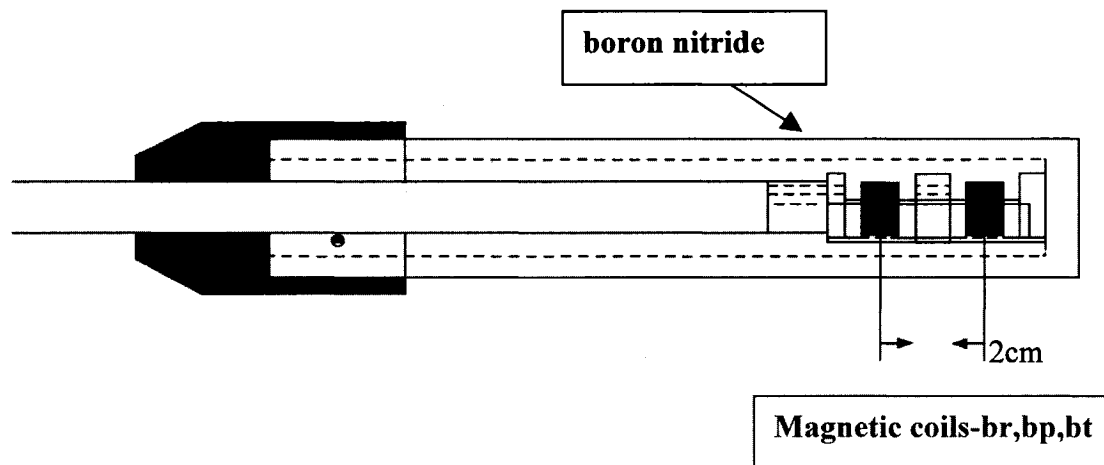


Figure 2.4. Schematic of the B-dot probe

The movable b-dot probe also needs calibration for the effective area of each coil and alignment because the imperfect alignments cause coils, designed to measure  $B_t$  (toroidal magnetic field) or  $B_p$  (poloidal magnetic field) signal only, to measure a mixture of  $B_t$  and  $B_p$  instead. There are two kinds of calibration for the b-dot probe. One is for the effective area  $A$ , and the other is for the coil alignment. Attenuation of signals due to the thickness of the electrostatic shielding, tension of wire on the coil form, and imprecision in winding deviates the value of the effective area  $A$  from such a simple relation ( $A=Na$ ). The effective area is calibrated with a Helmholtz coil [4] set that produces a known magnetic field. We should apply this method to each coil in the b-dot probe.

$$V_p = \frac{\partial \Phi}{\partial t} \approx 2\pi f N A B \quad (2.4)$$

Here  $f$  is the frequency,  $B$  is the known magnetic field, and  $V_p$  is the probe-measured voltage. The effective area ( $NA$ ) of each coil is shown in Table 2.2.

Bp coils	$5.768 \text{ cm}^2$	$6.477 \text{ cm}^2$
Bt coils	$3.605 \text{ cm}^2$	$3.742 \text{ cm}^2$
Br coils	$13.428 \text{ cm}^2$	$13.938 \text{ cm}^2$

Table 2.2 Effective area of each component of coil triplets in movable b-dot probe

For the alignment correction, the b-dot probe is easier than the magnetic coil array, because we can change the direction of the probe. The three directions of coils of the probe are orthogonal to each other (see figure 2.5). Thus we need to align only one direction. It is easy to do Bt coil alignment using the vacuum Bt shots (or the vacuum field that exists prior to each RFP discharge) after we install the probe in MST. We can check the alignment by changing the orientation of the probe shot by shot.

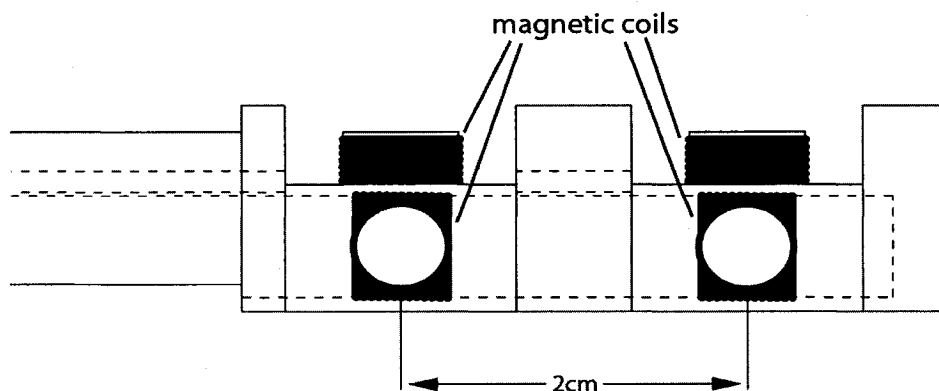


Figure 2.5 Magnification of magnetic coil triplets in B-dot probe

The Br coil calibration needs more careful manipulation because the flux surfaces are not concentric with the vacuum vessel (except at  $r = a$ ) but are instead shifted (Shafranov shift [6] due to the effect of toroidicity) outward from the geometric axis of the machine (Figure 2.6). This means that when two probes at different poloidal angles are inserted the same distance from the wall, the probe, that is most outboard will be effectively deeper in the plasma than others. Imperfect alignments (shifted flux surface outward from the geometric axis of the machine) cause coils, designed to measure Br (radial magnetic field that is the field perpendicular to a magnetic surface) signal only, to measure  $k \cdot Br + s \cdot B_p$  instead. From the calculation of outward shift (through the code 'MSTFIT'), the angle between the probe br coil axis and the flux surface is known and the  $B_p$  part in Br coil measurement could be subtracted.

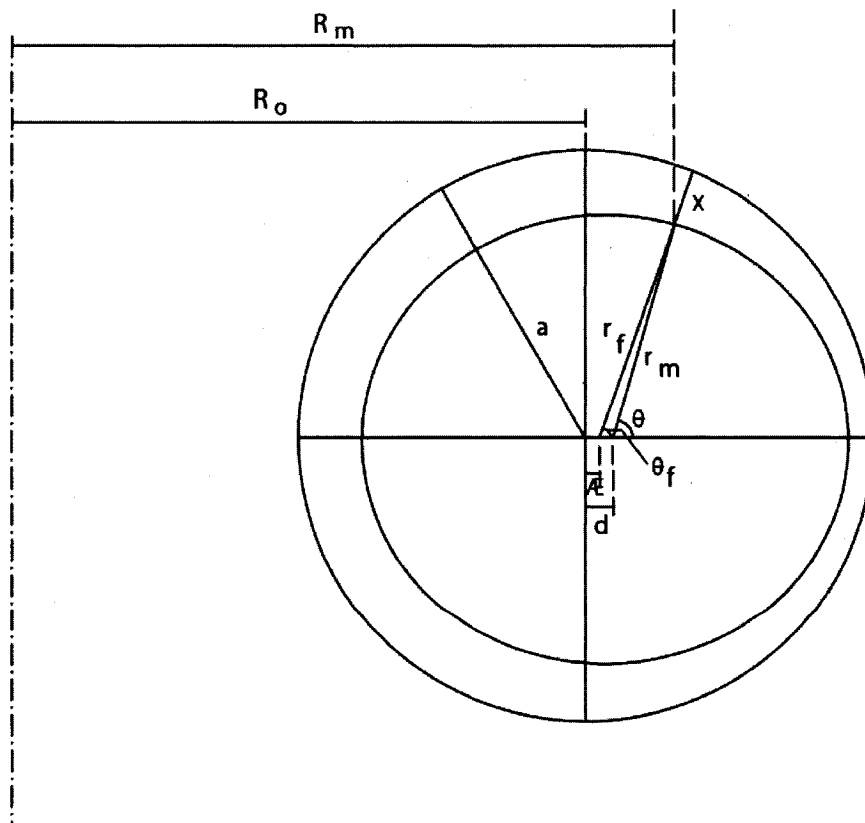


Figure 2.6. Schematic drawing of flux surface and MST geometry [7]

using MSTFIT, we find that the parameters in figure 2.6 for our conditions are  $d=6\text{cm}$ ,  $a=52\text{cm}$ ,  $\Delta=2\text{cm}$ ,  $\theta=5\pi/12$  radian,  $r_m=50.12\text{cm}$ . for a probe depth  $x$  cm, we have

$$\tan \theta_f = \frac{(50.1231 - x) \sin(5\pi/12)}{(50.1231 - x) \cos(5\pi/12) + 4} \quad (2.5)$$

From equation 2.5, we could find out the angle between the poloidal magnetic field and the radial magnetic field at the depth of probe ( $x$ ). The angle between them is  $5\pi/12 - \theta_f$  at our probe location. The measured radial magnetic field should be corrected by subtracting poloidal magnetic field pickup ( $=b_p \cdot \sin[5\pi/12 - \theta_f]$ ) at the location of probe. The correction to the radial magnetic field in different radial points is shown in Table 2.3.

6.5cm	6cm	5.5cm	5cm	4.5cm
Br-	Br-	Br-	Br-	Br-
0.0861948*Bp	0.0852475*Bp	0.0843206*Bp	0.0834136*Bp	0.0825258*Bp

Table 2.3 Calibration of radial component of magnetic field at various radial depth

#### 2.4 Movable triple Langmuir probe

The triple Langmuir probe is needed to measure the electron temperature and the floating potential. Figure 2.7 shows the schematics of triple Langmuir probe. The molybdenum and the boron nitride are chosen to survive in the high heat load environment inside MST [3]. The probe dimension has to be considered for overheating and perturbation on the global plasma [3,8].

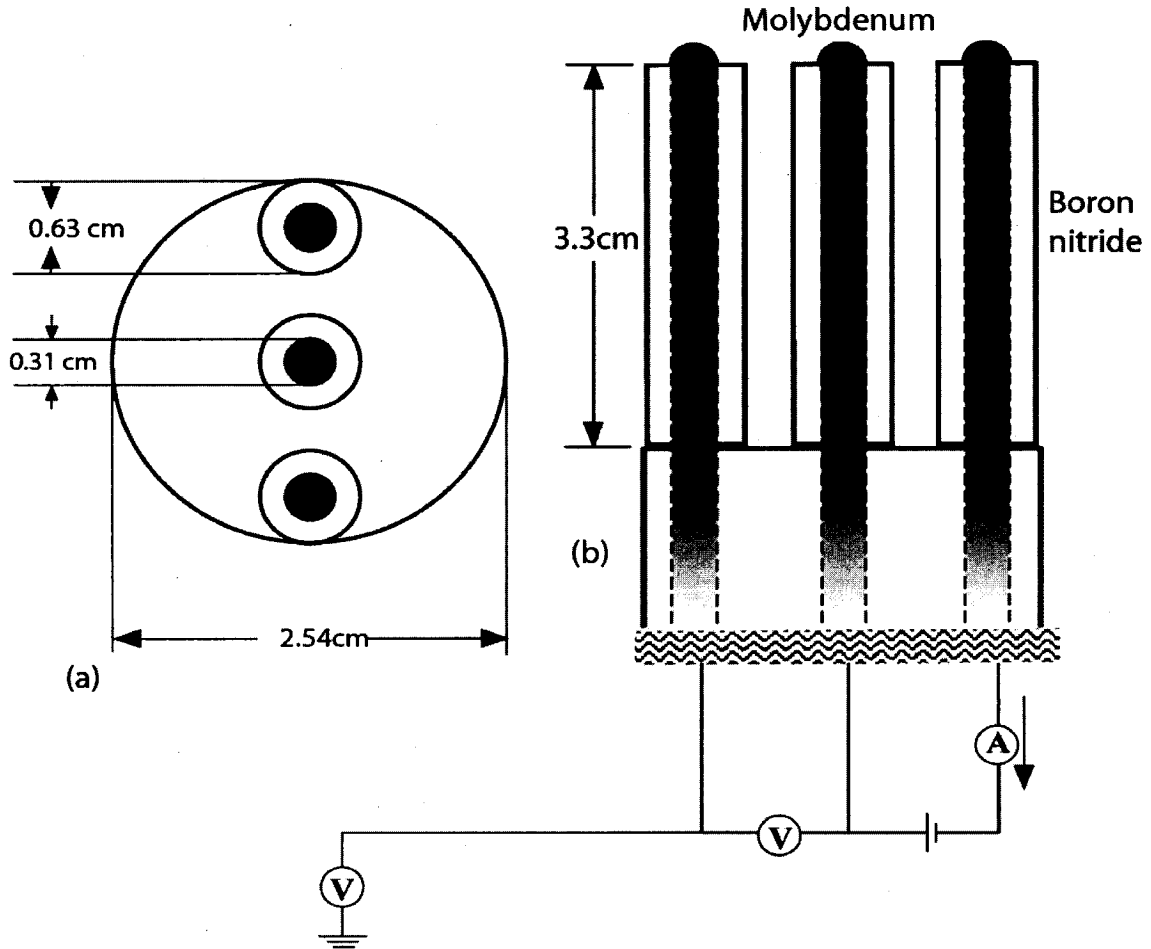


Figure 2.7 Langmuir probe used to measure floating potential, showing top view (left) and side view (right).

Three conductors are used simultaneously with fixed biased voltage on two of them. We assume that the same probe characteristic curve (I-V curve) applies to all probe tips. Two of them are biased with respect to each other, but are insulated from ground.

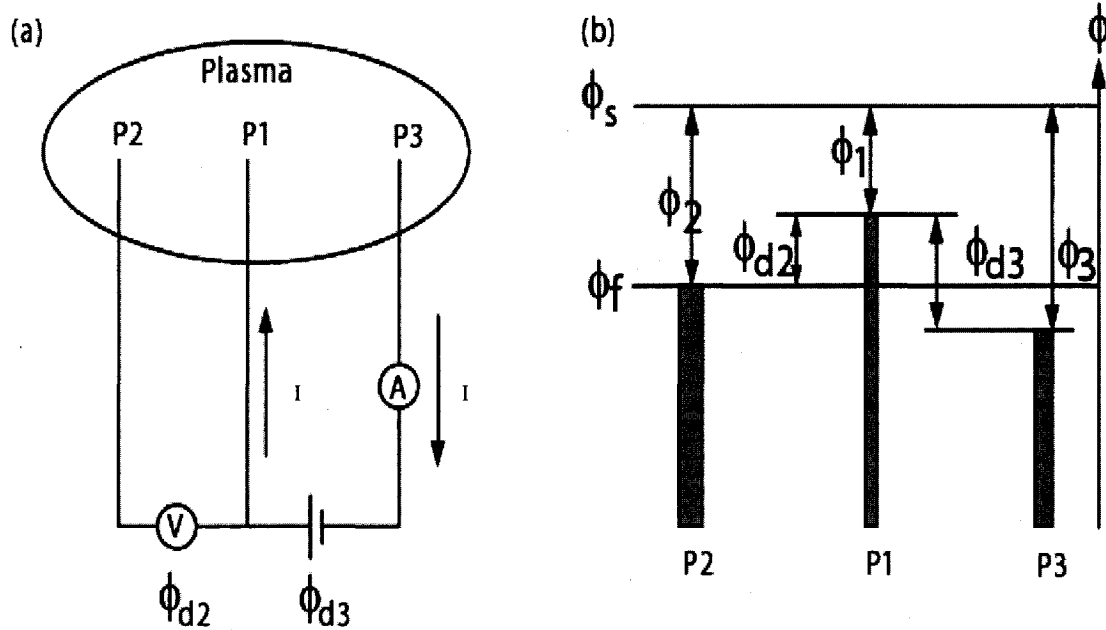


Figure 2.8 (a) Simplified probe circuit, (b) Potential of each probe [3]

Figure 2.8 demonstrates the simplified triple-probe circuit and electric potential of each probe. Probes P1, P2, and P3 are inserted into the plasma. As described above, P1 and P3 are biased with respect to each other with voltage  $\phi_{d3}$ , while P2 is floating. The potential location in the I-V curve of each probe is shown in figure. 2.8(b). Combined with the potential relation and I-V curve equation, we can have the equation for  $T_e$ .

$$\frac{1}{2} = \frac{1 - \exp(-\phi_{d2}/T_e)}{1 - \exp(-\phi_{d3}/T_e)} \quad (2.6)$$

Plasma density may be inferred by the equation (2.6) and I-V curve equation.

$$n_e = \frac{\exp(1/2)I_+}{A_+ e} \sqrt{\frac{m_i}{T}} \quad (2.7)$$

with  $I_+ = \frac{I}{1 - \exp((\phi d_2 - \phi d_3)/T)}$  and  $A_+$  is the area of ion collection, and  $m$  is ion

mass. The relation between floating potential ( $\phi_f$ ) and plasma potential( $\phi_p$ ) is

$$\phi_p = \phi_f + \alpha T$$

where (2.8)

$$\alpha = \left[ \frac{1}{2} + \ln\left(\frac{A_-}{A_+} \sqrt{\frac{m_i}{2\pi m_e}}\right) \right]$$

In order to minimize the noise of measurement of triple Langmuir probe, the power supply box should be constructed carefully. The bandwidth of the electronics used is around 50 kHz and the time lag between input signal and output signal is 10  $\mu$ sec.

#### References

1. S.L. Chen *et al.*, J. Appl. Phys. **36**, 2363 (1965)
2. H. Toyama *et al.*, Rev. Sci. Instrum. **62**, 2326 (1991)
3. C. Chiang, Ph.D thesis, University of Wisconsin, Madison, 2000
4. W. Shen, Ph.D thesis, University of Wisconsin, Madison, 1999
5. A. Almagri, private communication (2004)
6. V.D. Shafranov, Plasma Phys. **13**, 757 (1971)
7. D. Craig, Ph.D thesis, University of Wisconsin, Madison, 1998
8. D. Gibbons, Thermionic Emission in Handbooks of Vacuum Physics, Pergamon (1966)

### 3. Analysis Methods

The analysis methods used in our research are explained in this chapter including the m, n mode identification from one point measurements and the bi-spectrum. The m,n spectra of the boundary magnetic field is provided straightforwardly from the coil array (Sec. 3.1). However, to infer m,n spectra from internal single point measurements we have extended a technique long used in MST research. The technique is described in Section 3.3, following a description of ensemble averaging (Sec. 3.2). ensemble averaging is essential to the technique and to all of our results. Bi-spectra are evaluated to measure three-wave coupling and described in Section 3.4. The noise analysis for various order correlation is described in the appendix of this report.

#### 3.1 Identification of poloidal and toroidal mode numbers at the boundary

Only the toroidal mode number n can be detected by the toroidal array of coils in the experiment. To obtain the poloidal mode number the relation between poloidal magnetic field ( $B_\theta$ ) and toroidal magnetic field ( $B_\phi$ ) should be used to arrive at the poloidal mode number m for a given measured toroidal mode number n. At the boundary of MST, the radial component of current is almost zero because MST has a vacuum layer between the plasma and the vacuum vessel. Thus,

$$\begin{aligned}
 j_r &= 0 \\
 \rightarrow (\nabla \times \vec{b})_r &= 0 \\
 \rightarrow \frac{1}{r} \frac{\partial b_\phi}{\partial \theta} - \frac{\partial b_\theta}{R \partial \phi} &= 0
 \end{aligned} \tag{3.1}$$

A cylindrical coordinate system with  $z = R\phi$  is used here from the transformation of coordinate system because the toroidal magnetic field is small at the edge of MST [1]. By the assumption about the fluctuation magnetic field b,



$$b \sim \exp[i(\underline{k} \cdot \underline{r})] = \exp[i(k_\theta r\theta + k_\phi R\phi)] \quad (3.2)$$

and by the periodicity with  $2\pi$  in the poloidal and the toroidal angles, we identify mode number  $m, n$  as

$$k_\theta = \frac{m}{r}, k_\phi = \frac{n}{R}$$

From equation (3.1), we find  $\frac{m}{a} b_\phi = \frac{n}{R} b_\theta$ . The ratio  $a/R$  is about 0.35 in MST. We get

the following equation for the magnetic fluctuations at the wall.

$$\frac{b_\theta}{b_\phi} = 2.9 \frac{m}{n} \quad (3.3)$$

Thus, the  $m=0$  modes do not have a  $b_\theta$  field at the plasma boundary in the cylindrical approximation. The  $m=1$  modes could have both  $b_\theta$  and  $b_\phi$ .

For resonant modes, which are expected to be dominant, the wave number  $k$  satisfies  $k \cdot B_0 = 0$ , or

$$-\frac{m}{n} = \frac{rB_\phi}{RB_\theta} \quad (3.4)$$

The safety factor  $q = \frac{rB_\phi}{RB_\theta}$ , so modes are resonant where  $q = -\frac{m}{n}$ . Figure 1.2 show the  $q$

profile for a typical MST plasma and the location of several resonant surfaces.

Modes with  $m=1,2,3$  and  $|n| \leq 4$  cannot be resonant modes in MST because the  $q$  is less than 0.25. This means that  $n=-1,-2,-3,-4$  modes are dominated by  $m=0$ . From this reasoning,  $b_\phi$  for  $n=-1,-2,-3,-4$  from the toroidal coil array should have the poloidal mode number  $m=0$  and  $b_\theta$  for  $n=-6,-7,-8,-9\dots$  should have the poloidal mode number  $m=1$ .

Since  $b_\phi$  is sensitive to  $m=0$  but  $b_\theta$  is not (equation 3.3) the  $b_\phi$  spectrum has significantly more power at  $n=-1 \sim -4$  than the  $b_\theta$  (figure 2.2 and 2.3). As mentioned previously, the  $m=0$  modes are called edge modes because they are resonant near the edge and the  $m=1$  modes are called core modes because they are resonant near the core. From these considerations, we see that the dominant resonant modes are as in table 2.1.

### 3.2 Ensemble Averages

This section details the techniques employed to produce the ensemble quantities presented in this project. Ensemble-averaging is necessary in our analysis to infer spatial averages from single point measurements. The toroidal and poloidal angular average is needed to measure the terms in the MHD energy equation.

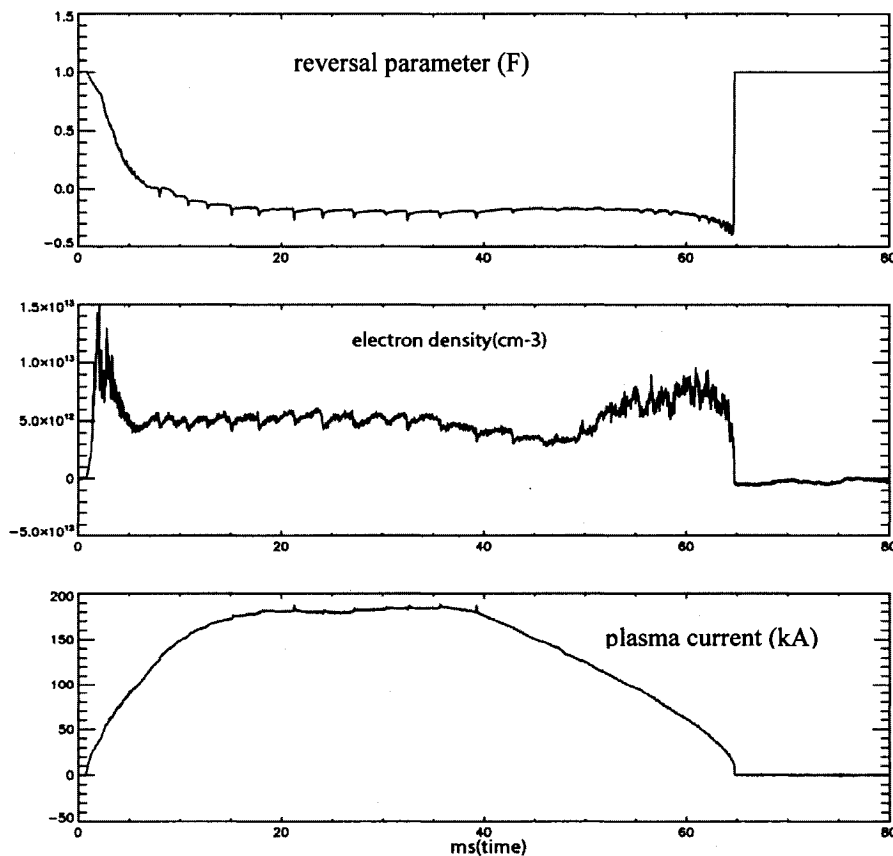


Figure 3.1 Global plasma parameters used to choose the ensemble

Ensemble averages replace the magnetic surface averages (toroidal and poloidal). This is valid if the modes are rotating so that different elements in the ensemble sample different mode phases. The ensembles presented in this study are selected from the flat-top region of many similar discharges. The plasma current, reversal parameter, electron density (figure 3.1) and rotation (of the  $n=6$  mode) are considered to choose the similar discharges. To compose an ensemble of sawtooth cycles individual events are selected for each shot of interest. The IDL software has been developed by the MST group to analyze signals over a carefully constrained sawtooth ensemble. It is described in references [2,3]. A number of routines operate together to accomplish the generation of an ensemble. The first routine generates a simple shot list containing the shot-number, date of each discharge and times indicating the portion of the discharge to be analyzed. The crash points in discharge time are selected to make an ensemble in the normal sawtooth plasmas and the enhanced confinement plasmas. The increasing mode midpoints in slow growth QSH discharge are also selected to make the ensemble. After creating the ensemble, a second routine is run to characterize each event by the various discharge parameters at the time of the event. After the above process, the ensemble parameters are bounded to exclude outliers and constrain the ensemble to consist of similar events. Finally, we can make different size of ensembles at each case: 1000 normal sawtooth crashes, 350 enhanced confinement bursts, and 100 slow growth QSH.

### **3.3 Identification of modes from one point internal measurements**

We cannot identify  $m$  and  $n$  directly from an one point measurement, such as a single magnetic or Langmuir probe measurement inside MST. We need multiple point measurements to deduce  $m$  and  $n$  spectra. For many years, the MST group has estimated

the  $k$  spectrum of a quantity within the plasma by correlating the single point measurement with various spatial Fourier modes measured with the edge array of magnetic probes. This technique produces the component of the internal signal that is correlated with the quantity at the edge. It would not produce information on  $k$  spectra of quantities that are localized within the plasma and vanish at the edge.

For the  $m=0$  and  $m=1$  tearing modes, the magnetic field is nonzero at the plasma edge; thus this technique should produce useful  $k$  spectra of the quantity within the plasma. Within the MST group these  $k$  spectra are referred to as “pseudospectra”. One limitation in the technique is that it relies on mode rotation, such that an ensemble average is equivalent to a toroidal average. In that case, a Fourier harmonic that is present in the internal signal will only correlate with a harmonic at the edge at the same mode number. However, if the modes are not perfectly rotating, then the ensemble average is not a perfect toroidal average. In that case, the correlation in time between different Fourier modes at the edge will be nonzero, producing an error in the deduced  $k$  spectrum of the internal signal. We have devised a modification to the standard technique to eliminate this error (for cases where the error is not large). Below we describe the standard pseudospectrum technique, followed by the modified technique.

### **Standard pseudo-spectrum technique**

The  $m$  and  $n$  modes of a quantity  $\Phi(r, \vartheta, \varphi, t)$  inside MST can be measured in the following way. We decompose  $\Phi(r, \vartheta, \varphi, t)$  into its Fourier modes with coefficients  $\phi(r, t)_{m,n}$ :

$$\Phi_{total}(r, \vartheta, \varphi, t) = \sum_{m,n} \phi(r, t)_{m,n} e^{i(m\vartheta+n\varphi)}$$

The Fourier coefficients  $\phi(r, t)_{m,n}$  can be divided into two parts. One is correlated with the magnetic field fluctuation at the plasma boundary and the other is not.

$$\begin{aligned}\phi(r, t)_{m,n} &= \phi(r, t)_{m,n}^{correlated} + \phi(r, t)_{m,n}^{uncorrelated} \\ \phi(r, t)_{m,n}^{correlated} &= \frac{c_{m,n} b_{m,n}}{|b_{m,n}|}\end{aligned}\quad (3.5)$$

Here,  $b_{m,n}$  is one complex Fourier component of the magnetic fluctuation at the edge of MST derived from the 64 toroidal coil array. The unknown  $c_{m,n}$ , which is in the  $\phi(r, t)_{m,n}^{correlated}$ , can be formed from the known  $b_{m,n}$  and  $\Phi_{total}(r, \vartheta, \varphi, t)$ .

$$\left\langle \Phi_{total}(r, \vartheta, \varphi, t) \cdot b_{p,q}^* e^{-i(p\vartheta+q\varphi)} \right\rangle = \sum_{m,n} c_{m,n} \left\langle \frac{b_{m,n} e^{i(m\vartheta+n\varphi)}}{|b_{m,n}|} \cdot b_{p,q}^* e^{-i(p\vartheta+q\varphi)} \right\rangle$$

The bracket  $\langle \rangle$  means the toroidal and poloidal average. Now we can apply the orthogonality relation for  $b_{m,n}$

$$\left\langle b_{m,n} \cdot b_{p,q}^* e^{i(m\vartheta+n\varphi)} e^{-i(p\vartheta+q\varphi)} \right\rangle = |b_{m,n}|^2 \delta(m-p) \delta(n-q) \quad (3.6)$$

From this orthogonality relation, we can find the unknown  $c_{m,n}$ :

$$c_{m,n} = \frac{\left\langle \Phi_{total} * b_{m,n}^* e^{-i(m\vartheta+n\varphi)} \right\rangle}{|b_{m,n}|}$$

The  $\phi(r, t)_{m,n}^{uncorrelated}$  is deleted when  $b_{m,n}$  is applied because it is not correlated with magnetic field. If the modes rotate well then we can use an ensemble average to approximate the toroidal and poloidal average. Let  $\Phi(r, \bar{\vartheta}, \bar{\varphi}, t)$  be a measurement at a single point at a specific toroidal and poloidal angle  $(\bar{\vartheta}, \bar{\varphi})$ . Then the unknown  $c_{m,n}$  becomes:

$$c_{m,n} = \frac{\langle \Phi * b_{m,n}^* \rangle e^{-i(m\bar{g}+n\bar{\varphi})}}{|b_{m,n}|}$$

The bracket  $\langle \rangle$  means the ensemble average.

### Modified pseudospectrum technique

In the real experiment, the rotation of each mode is not always good enough for equation 3.6 to strictly apply. Therefore an error is introduced in estimating each spectrum from the standard technique because the orthogonality relation is not completely satisfied. Figure 3.2 presents the phase distribution of  $m=0, n=1$  mode during the sawtooth crash ensemble. If the mode rotates well, the histogram should be flat (even distribution of phase). The orthogonality relation is strictly satisfied only for an even phase distribution. In real experiments the phase distribution is not perfectly flat as you can see in figure 3.2.

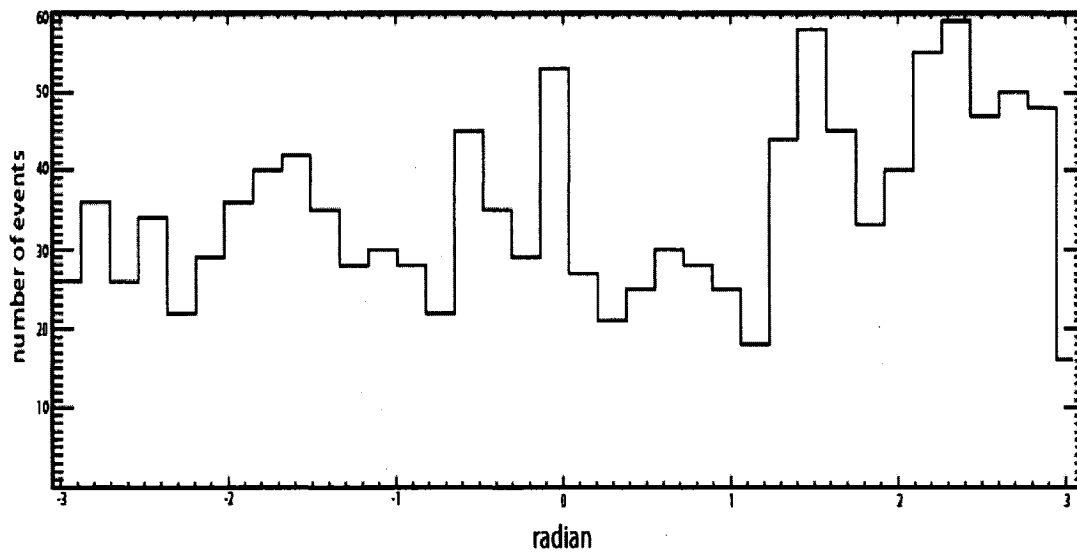


Fig 3.2 Histogram of  $m=0, n=1$  mode phases at sawtooth crash

The matrix equation below shows the ideal case (orthogonality satisfied) using the standard technique in a specific mode number  $m$ . The ideal case gives us a diagonal matrix to solve the  $c_{m,n}$ .

$$\begin{pmatrix} \langle \Phi \cdot b_{m,0}^* \rangle \\ \langle \Phi \cdot b_{m,1}^* \rangle \\ \dots \\ \dots \\ \dots \\ \langle \Phi \cdot b_{m,n}^* \rangle \end{pmatrix} = \begin{pmatrix} \langle |b_{m,0}|^2 \rangle^{1/2} e^{i(m\vartheta)} & 0 & 0 & 0 \\ 0 & \langle |b_{m,1}|^2 \rangle^{1/2} e^{i(m\vartheta+\varphi)} & 0 & 0 \\ 0 & 0 & \dots & 0 \\ \dots & \dots & \dots & \dots \\ 0 & 0 & 0 & \langle |b_{m,n}|^2 \rangle^{1/2} e^{i(m\vartheta+n\varphi)} \end{pmatrix} \begin{pmatrix} c_{m,0} \\ c_{m,1} \\ \dots \\ \dots \\ \dots \\ c_{m,n} \end{pmatrix}$$

The modified technique that we developed includes the correlation between modes due to slow or non-uniform rotation. From this, we can reduce the errors caused by the slow rotation. By the multiplication of complex conjugate of the  $b_{m,n}$  into  $\Phi(r, \vartheta, \varphi, t)$ , we can get the  $n+1$  by  $n+1$  matrix at each specific  $m$  value. From this  $n+1$  by  $n+1$  matrix we can solve for the unknown  $c_{m,n}$  at the specific poloidal mode number  $m$  ( $m=0,1,2,3\dots$ ).

$$\begin{pmatrix} \langle \Phi \cdot b_{m,0}^* \rangle \\ \langle \Phi \cdot b_{m,1}^* \rangle \\ \dots \\ \dots \\ \dots \\ \langle \Phi \cdot b_{m,n}^* \rangle \end{pmatrix} = \begin{pmatrix} \langle |b_{m,0}|^2 \rangle^{1/2} e^{i(m\vartheta)} & \frac{\langle b_{m,1} \cdot b_{m,0}^* \rangle}{\langle |b_{m,1}|^2 \rangle^{1/2}} e^{i(m\vartheta+\varphi)} & \dots & \frac{\langle b_{m,n} \cdot b_{m,0}^* \rangle}{\langle |b_{m,n}|^2 \rangle^{1/2}} e^{i(m\vartheta+n\varphi)} \\ \frac{\langle b_{m,0} \cdot b_{m,1}^* \rangle}{\langle |b_{m,0}|^2 \rangle^{1/2}} e^{i(m\vartheta)} & \langle |b_{m,1}|^2 \rangle^{1/2} e^{i(m\vartheta+\varphi)} & \dots & \frac{\langle b_{m,n} \cdot b_{m,1}^* \rangle}{\langle |b_{m,n}|^2 \rangle^{1/2}} e^{i(m\vartheta+n\varphi)} \\ \dots & \dots & \dots & \dots \\ \dots & \dots & \dots & \dots \\ \frac{\langle b_{m,0} \cdot b_{m,n}^* \rangle}{\langle |b_{m,0}|^2 \rangle^{1/2}} e^{i(m\vartheta)} & \dots & \dots & \langle |b_{m,n}|^2 \rangle^{1/2} e^{i(m\vartheta+n\varphi)} \end{pmatrix} \begin{pmatrix} c_{m,0} \\ c_{m,1} \\ \dots \\ \dots \\ \dots \\ c_{m,n} \end{pmatrix}$$

Fortunately the careful investigation of the correlation between each mode at the edge of MST allows us to usually employ a 2 by 2 matrix instead of n+1 by n+1 matrix because only a few off-diagonal terms are dominant in the n+1 by n+1 matrix. For example, the m=1 and n=6 mode of the potential from the Langmuir probe measurement is from

$$\langle V * b_{1,6}^* \rangle = \frac{c_{1,6} \langle b_{1,6} * b_{1,6}^* \rangle}{\langle |b_{1,6}|^2 \rangle^{1/2}} e^{i(\vartheta+6\varphi)} + \frac{c_{1,7} \langle b_{1,7} * b_{1,6}^* \rangle}{\langle |b_{1,7}|^2 \rangle^{1/2}} e^{i(\vartheta+7\varphi)} \quad (3.7)$$

$$\langle V * b_{1,7}^* \rangle = \frac{c_{1,6} \langle b_{1,6} * b_{1,7}^* \rangle}{\langle |b_{1,6}|^2 \rangle^{1/2}} e^{i(\vartheta+6\varphi)} + \frac{c_{1,7} \langle b_{1,7} * b_{1,7}^* \rangle}{\langle |b_{1,7}|^2 \rangle^{1/2}} e^{i(\vartheta+7\varphi)}$$

This gives a 2 by 2 matrix for two unknown  $c_{1,6}$  and  $c_{1,7}$ . In the above equation (equation 3.7),  $b_\theta$  with n=6 and 7 could be used for  $b_{1,6}$  and  $b_{1,7}$  because we already know that the  $b_\theta$  with n=6 and 7 should have the poloidal mode number m=1 (see Section 3.1). In making the matrix, the degree of correlation between modes is investigated carefully to choose the most important terms.

### 3.4 Bi-spectrum

The bi-spectrum is a powerful statistical concept to analyze data associated with various nonlinear phenomena, including nonlinear wave coupling [4]. To distinguish between nonlinear-coupled waves and linear independent waves, a higher order spectrum, the bi-spectrum, is needed. It measures the degree of phase coherence between waves. This technique successfully identified three-wave interaction in fluids [5,6] and nonlinear energy cascading in edge plasma fluctuations [7]. Plasmas in the MST are ideally suited



for investigating nonlinear wave-wave processes since the largest amplitude fluctuations strongly interact, and these fluctuations are well resolved using the toroidal coil array at the plasma surface. The bi-spectrum was applied to magnetic fluctuations in MST previously [8] although the quality of the toroidal array data has substantially improved since that time. Applying the statistical method and the discrete Fourier transform (DFT), we can find the bi-spectrum for the magnetic fluctuations. Skipping many steps for the sampling and DFT, we obtain the following definitions for bi-spectrum [9].

$$\gamma^2[n_1, n_2] = \frac{\langle |b_{n_1}^* b_{n_2}^* b_{n_1+n_2}| \rangle^2}{\langle |b_{n_1+n_2}|^2 \rangle \langle |b_{n_1} b_{n_2}|^2 \rangle} \quad (3.8)$$

The  $b_{n_1}$  is a magnetic fluctuation with mode number  $n_1$ .

### **Statistical meaning of Bi-Spectrum**

Let us suppose that two waves at wave numbers  $n_1$  and  $n_2$  interact nonlinearly to form a sum wave number  $n_3$ , i.e.,  $n_1 + n_2 = n_3$ . The corresponding Fourier amplitudes  $x_{n_1}, x_{n_2}, x_{n_3}$  may be modeled by the relationship,

$$x_{n_3} = A \cdot x_{n_1} x_{n_2} + \varepsilon \quad (3.9)$$

where  $A$  is a measurement of the strengths of the coupling and  $\varepsilon$  denotes any statistically independent errors associated with the imperfection of the model and a real independent part. In more physical terms, if the nonlinear interaction of two waves at wave number  $n_1$  and  $n_2$  gives rise to a new wave at wave number  $n_3 = n_1 + n_2$ , there will be a phase correlation (phase locking) between the three waves. The bi-spectrum is a measurement of this phase correlation and is a very useful concept with which to detect nonlinearities

in fluctuation data. In order to clarify the physical meaning of “partially coupled”, we consider the total power at wave number  $n_3$ .

That is,

$$P(n_3) = \langle |x(n_3)|^2 \rangle = |A|^2 \langle |x(n_1)x(n_2)|^2 \rangle + \langle |\varepsilon|^2 \rangle \quad (3.10)$$

The first part in RHS of equation 3.10 is the power from coupling of  $x[n_1]$  and  $x[n_2]$ .

From above definition of bi-spectrum, we obtain

$$\begin{aligned} \gamma^2 &= \frac{\langle |x_{n_3} x_{n_1}^* x_{n_2}^*|^2 \rangle}{\langle |x_{n_1} x_{n_2}|^2 \rangle \langle |x_{n_3}|^2 \rangle} \\ &= \frac{|A|^2 \langle |x_{n_2} x_{n_1}|^2 \rangle^2}{\langle |x_{n_2} x_{n_1}|^2 \rangle \langle |x_{n_3}|^2 \rangle} = \frac{|A|^2 \langle |x_{n_2} x_{n_1}|^2 \rangle}{\langle |x_{n_3}|^2 \rangle} \end{aligned} \quad (3.11)$$

Therefore, the bi-spectrum represents the fraction of power at wave number  $n_3 = n_1 + n_2$  due to the coupling of waves at wave numbers  $n_1$  and  $n_2$  (Eq. 3.10).

### **Selection Rule in Bi-spectrum**

The bi-spectrum between modes follows the selection rule ( $n_1 + n_2 = n_3$ ). We find coupling in MST (figure 3.3(a)) for the triplet of modes with  $(m, n) = (0,1), (1,6), (1,7)$ , which satisfies the selection rule in both poloidal mode number  $m$  and toroidal mode number  $n$ . The triplet shown in figure 3.3(b) does not satisfy the selection rule in the poloidal mode number  $m$  because it is between  $(1,6), (1,7), (1,13)$ . As a result, the bi-

spectrum is as small as the statistical error which is also shown in the figure. The method for determining the error is discussed in the appendix.

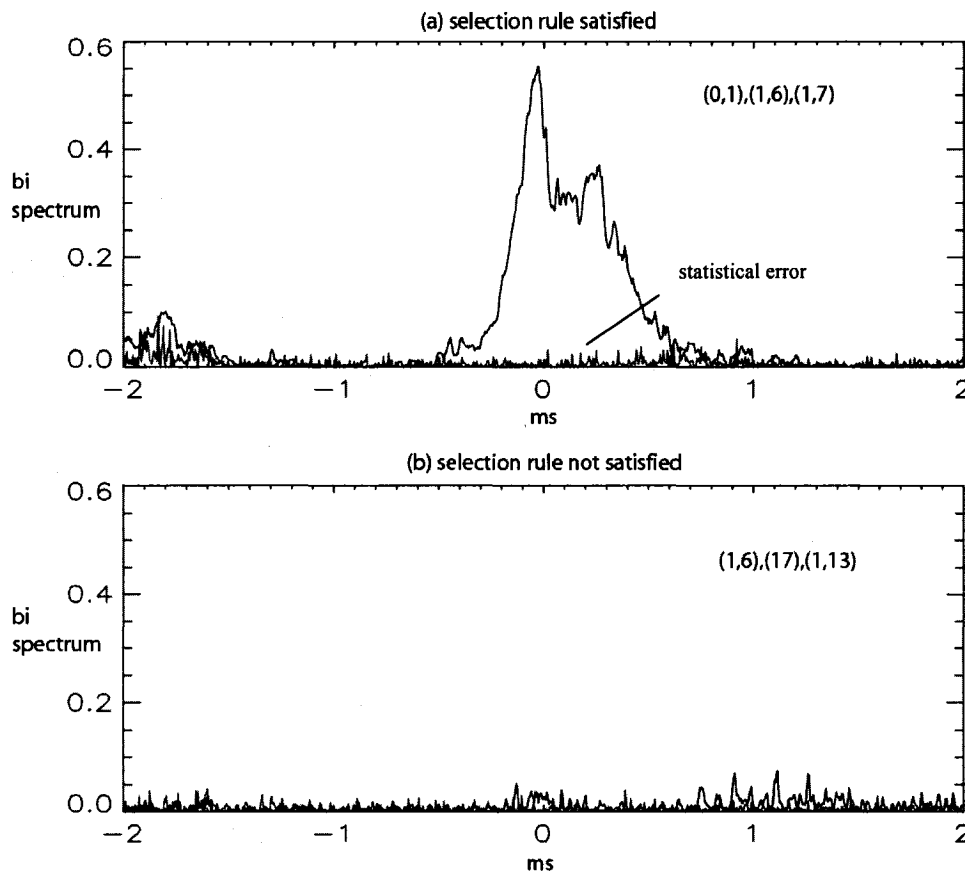


Figure 3.3 Bi-spectrum vs time through a sawtooth crash

### **Resonant mode and Non-Resonant mode in the bi-spectrum**

In this section, we provide some information about the nonlinear coupling between modes when the reversal parameter is larger than zero (non-RFP). In this case, the poloidal mode number  $m=0$  is not resonant (from safety factor profile). This means

that  $m=0$  modes are suppressed. The bi-spectrum for the triple  $(0,1), (1,6), (1,7)$  can still be measured and compared with that for the normal RFP.

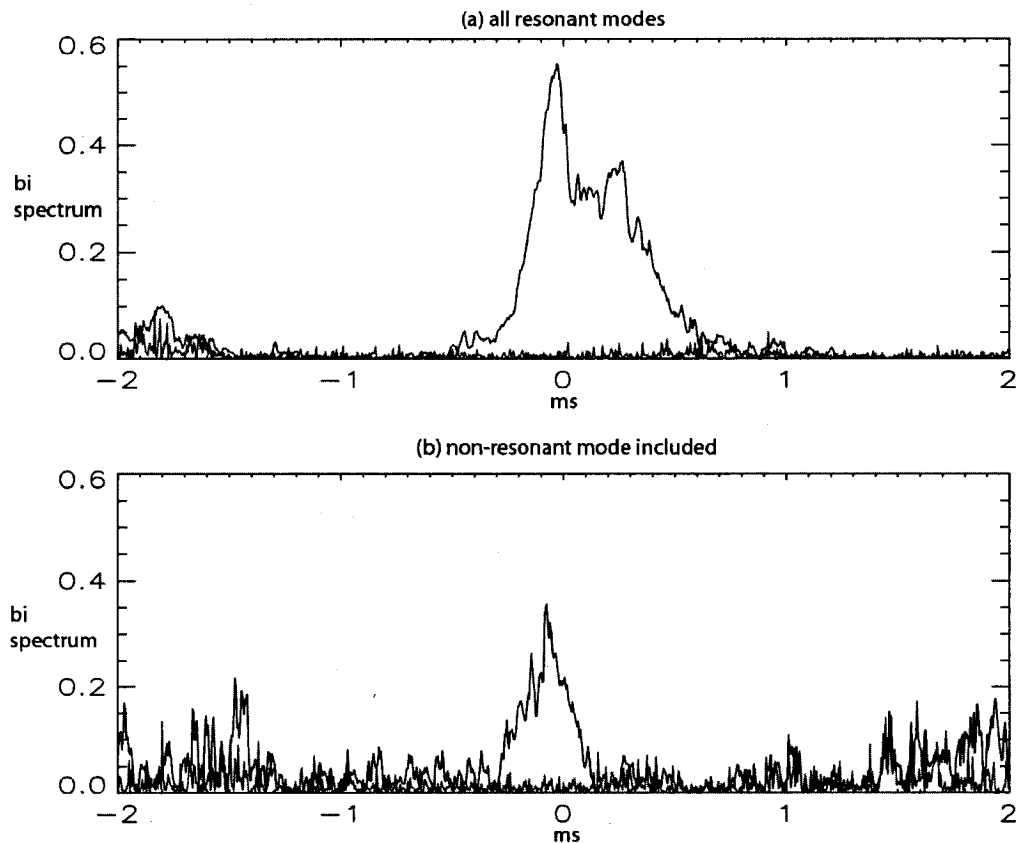


Figure 3.4 Bi-spectrum during a sawtooth crash in (a) normal RFP and (b) non-RFP for  $(0,1),(1,6),(1,7)$  interaction

Figure 3.4 (a) shows the bi-spectrum for the normal case where all modes are resonant along with the noise level. Figure 3.4 (b) shows the bi-spectrum in the non-RFP case where one mode is non-resonant ( $m=0$ ) and two modes are resonant ( $m=1$ ) along with a noise level. The bi-spectrum is larger in the normal RFP than in non-RFP. We can conclude that the coupling between resonant modes and non-resonant modes exists but appears to be weaker than in the case with all modes resonant.

### **Bi-spectrum of resonant modes with the same resonant surface**

The nonlinear coupling between resonant modes which are at the same resonant surface is shown in figure 3.5. Every  $m=0$  modes resonates at the same resonant surface (near the edge in MST). Figure 3.5 shows the bi-spectrum between (0,1), (0,2), (0,3) modes along with the noise level. These modes satisfy the selection rule.

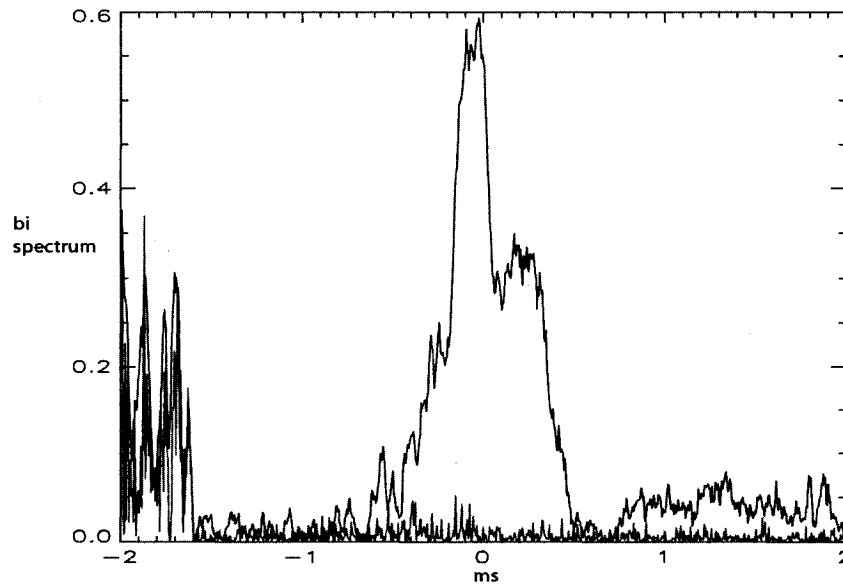


Figure 3.5 Bi-spectrum between (0,1), (0,2), (0,3) toroidal magnetic field modes

We conclude that in MST nonlinear coupling between resonant modes satisfying the selection rule exists for modes that share the same resonant surface, as well as for modes with different resonant surface.

### **References**

- 1 Jeffrey P. Freidberg, *Ideal Magneto Hydro Dynamics*, Plenum press (1987)
- 2 J.T. Chapman, Ph.D thesis, University of Wisconsin, Madison, 1998
- 3 J. Taylor, *Introduction to Error Analysis*, University Science Books (1982)
- 4 J.S. Sarff *et al.*, *Phys. Fluids B* **5**, 7 (1993)

- 5 R.W. Miksad *et al.*, *Phys. Fluids* **23**, 258 (1983)
- 6 S. Elgar *et al.*, *Fluid Mech.* **161**, 425 (1985)
7. C.P. Ritz *et al.*, *Phys. Fluids B* **1**, 153 (1989)
8. S. Assadi, Ph.D thesis, University of Wisconsin, Madison, 1992
- 9 E.J. Powers, *Intelligent Signal Processing* (1988)

## 4. Measurement of individual equilibrium and fluctuation quantities

### 4.1 Introduction

In this chapter, the equilibrium and fluctuation quantities measured by the probes (b-dot probe and Langmuir probe) in three different plasmas (Sawtooth, EC, QSH) are presented. Physic conclusions are drawn from products involving fluctuation and equilibrium quantities. We present a measurement of individual quantities (electric field, magnetic field, and velocity) in this chapter. The products are evaluated and key physics conclusion drawn in next chapter. We present three different plasmas in section 4.2. In section 4.3, we present the equilibrium measurement and in section 4.4 the fluctuation measurement is represented.

### 4.2 Three different plasmas-sawtooth , EC, and QSH

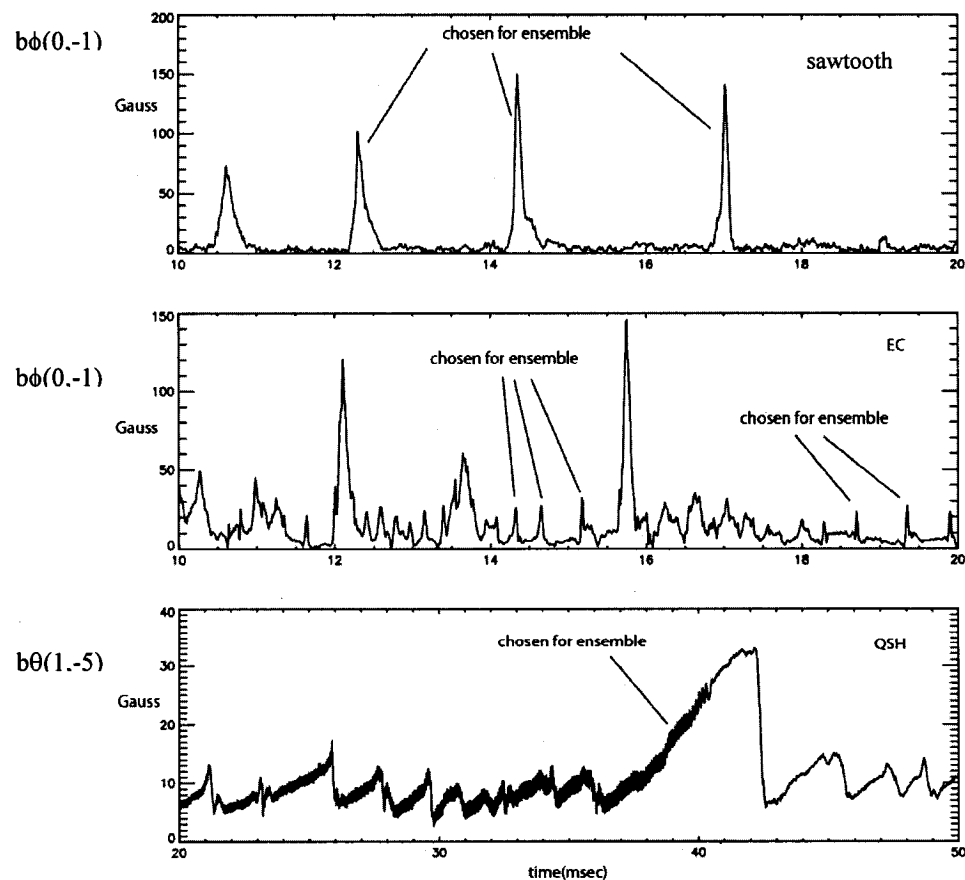


Figure 4.1 Magnetic fluctuation vs time, showing time periods used for ensemble-averaging in each case of plasmas

Figure 4.1 shows the amplitudes of magnetic fluctuation at the edge and how we pick the ensemble periods in three different plasmas (Sawtooth, EC, QSH). The large bursts of  $m=0$  magnetic fluctuations are chosen to make the sawtooth ensemble. The small bursts of  $m=0$  magnetic fluctuations between large bursts are chosen to make the ensemble for EC plasmas. The big and slow developing magnetic fluctuations are chosen to make the ensemble for QSH plasmas.

<b>Sawtooth</b>	C1-C4: 2200volts	C5:350volts	Bt crowbar:60volts
<b>EC</b>	C1, C2: 2500volts	C5 :110volts	Bt crowbar:90volts Bp crowbar:200volts
<b>QSH</b>	C1-C4 :2200volts	C5 :450volts	Bt & Bp crowbar: 0volts

Table 4.1 Parameters in each plasma (Sawtooth, EC, QSH)

Table 4.1 shows the parameters for the MST capacitors to make each plasma (Sawtooth, EC, QSH). The reversal parameter is  $\sim 0.2$  and electron density is  $0.5 * 10^{13} \text{ cm}^{-3}$  in the sawtooth plasma. The reversal parameter is  $\sim 0.5$  and electron density is  $0.5 * 10^{13} \text{ cm}^{-3}$  in the EC plasma. The reversal parameter is  $\sim 0$  and electron density is  $0.5 * 10^{13} \text{ cm}^{-3}$  in the QSH plasma. The electron density ( $\sim 0.5 * 10^{13} \text{ cm}^{-3}$ ) is optimized for fast mode rotation in MST to make ensemble analysis useful.



### 4.3 Measurements of equilibrium quantities

#### Triple Langmuir probe measurement

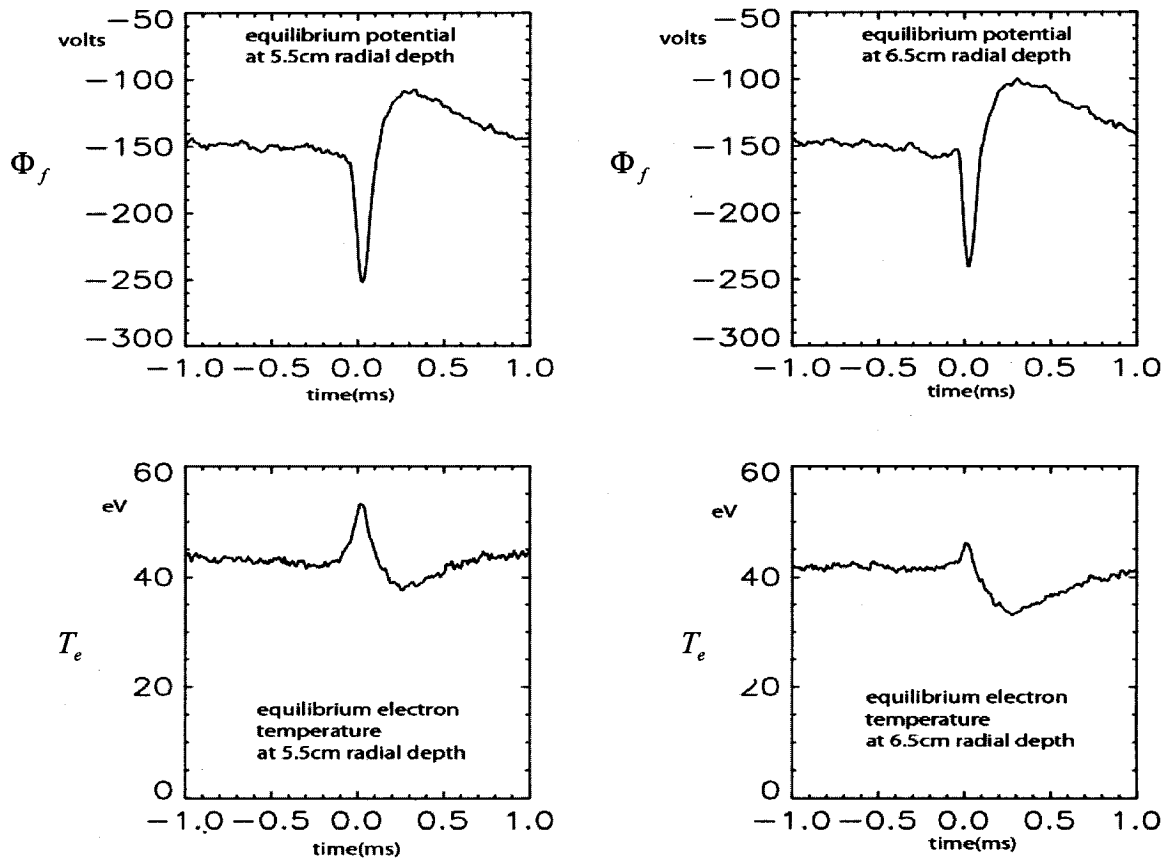


Figure 4.2 Equilibrium quantities (floating potential, electron temperature) during one sawtooth

In this section, the equilibrium quantities measured by the probes (b-dot probe and Langmuir probe) in three different plasmas (Sawtooth, EC, QSH) are presented. Physic conclusions are drawn from products involving fluctuation and equilibrium quantities. The equilibrium quantities are derived from the ensemble average over many similar events. The ensemble average is the same as toroidal and poloidal surface average because of mode rotation. Figure 4.2 shows the ensemble averaged floating potential and electron temperature (equilibrium quantities) during the sawtooth at two radial locations

in the edge of MST. The equilibrium floating potential is negative in the MST edge and has a very weak radial gradient at this location. The potential drops by about 100 V at the sawtooth crash. The equilibrium electron temperature is about 40 eV and increase slightly at the crash. The excitation of electron temperature at the sawtooth crash is less for the deeper insertion. The plasma potential is  $\Phi_p = \Phi_f + 2.2T_e$ . Hence given these measurements, the temperature correction is not negligible but small in the MST edge.

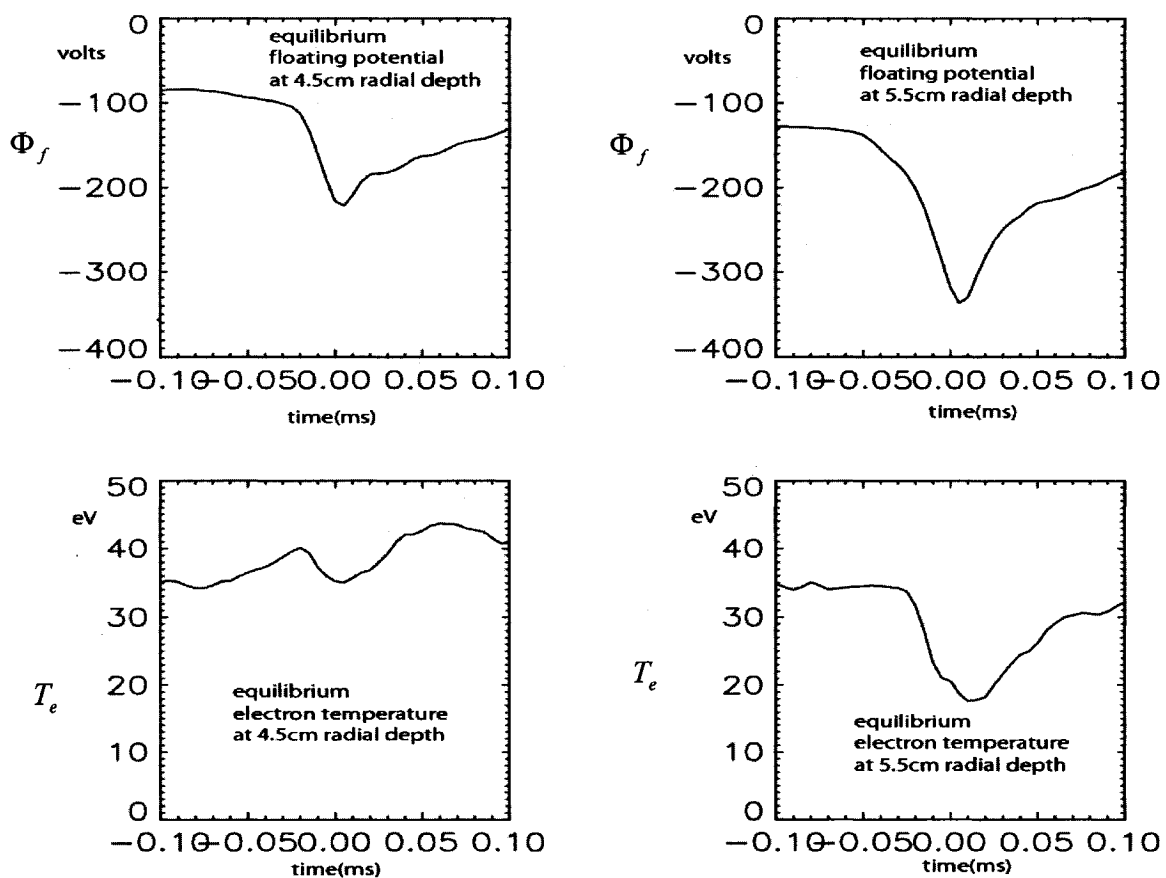


Figure 4.3 Equilibrium quantities (floating potential, electron temperature) during one EC burst

EC plasma has deeper reversal parameter than sawtooth plasma. This means that the reversal surface is located deeper inside MST. Figure 4.3 shows the ensemble

averaged floating potential and electron temperature during the EC burst. The cycle time of EC burst is much shorter than that of sawtooth. The equilibrium floating potential is negative in the MST edge and has a strong radial gradient at this location. The potential drops by about 150 V-200 V during the burst. This is more than for the sawtooth crash. The equilibrium electron temperature is about 40 eV and decreases during the burst. Therefore, the temperature correction for the electron potential in EC bursts is more negligible than for the sawtooth crash.

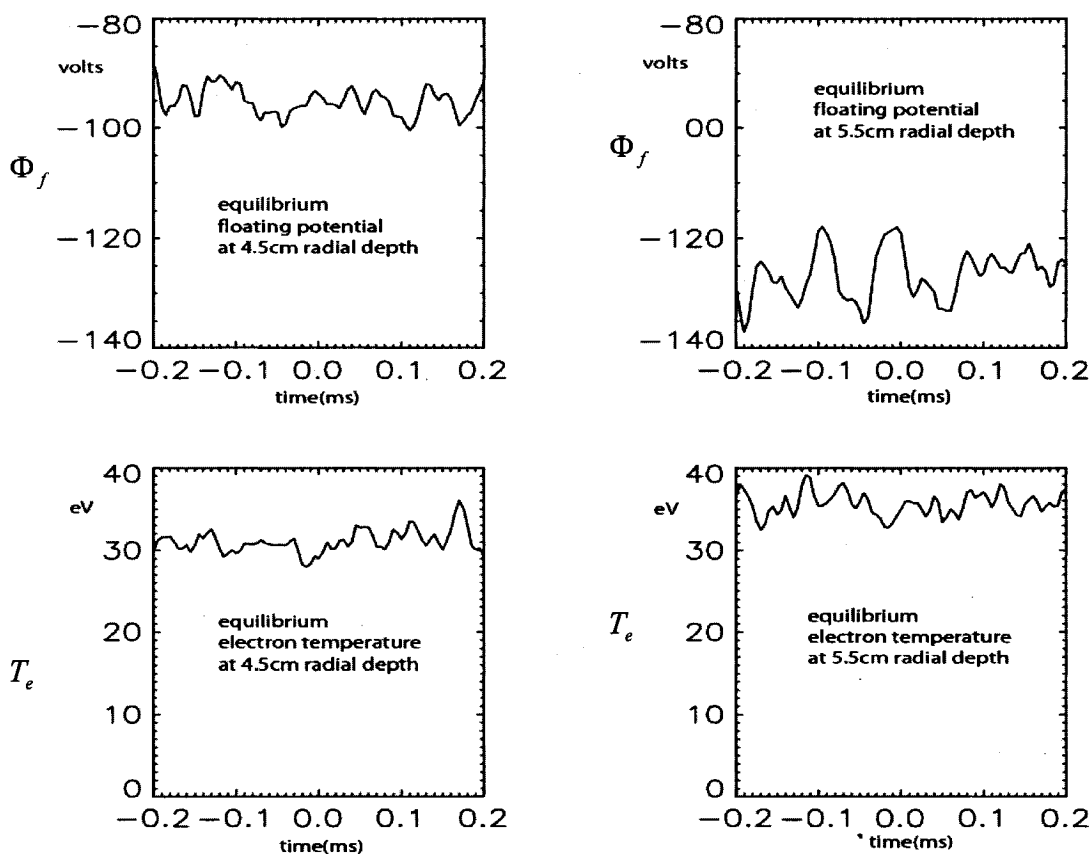


Figure 4.4 Equilibrium quantities (floating potential, electron temperature) during QSH

The modes in QSH plasma grow slowly compared to sawtooth or EC plasmas (see Fig. 4.1). Hence the time period in QSH used for ensemble averaging is different from other plasmas. The time period of faster part during the whole slow mode growing is selected. Figure 4.4 shows the ensemble averaged floating potential and electron temperature for the QSH plasma. There is not much change during the time window because the QSH periods are more steady-state and do not have a bursty character (see figure 1.7). The equilibrium floating potential is negative in the MST edge and has a radial gradient at this location. The equilibrium electron temperature is about 40 eV. Unlike other plasmas (RFP and EC), the magnitude of the floating potential is small and comparable with the electron temperature. Therefore, the temperature correction in QSH is not negligible, but important.

### **B-dot probe measurement**

Figure 4.5 shows the ensemble averaged components (radial, toroidal, and poloidal) of magnetic field at two radial points during the sawtooth. The equilibrium toroidal magnetic field is negative at edge of MST. The toroidal and poloidal equilibrium magnetic fields decrease with radius in the edge as expected from Taylor's theory (see Fig. 1.1). The poloidal equilibrium magnetic field is positive and is much larger than the other equilibrium magnetic field component. The radial field is a result of the probe not being aligned exactly perpendicular to the flux surfaces. Hence a fraction of the poloidal field is detected in the radial coil. The largest change at the crash is in the toroidal component which becomes less negative at both radii. It means the  $m=0$  resonant surface moves toward the wall at sawtooth crash.

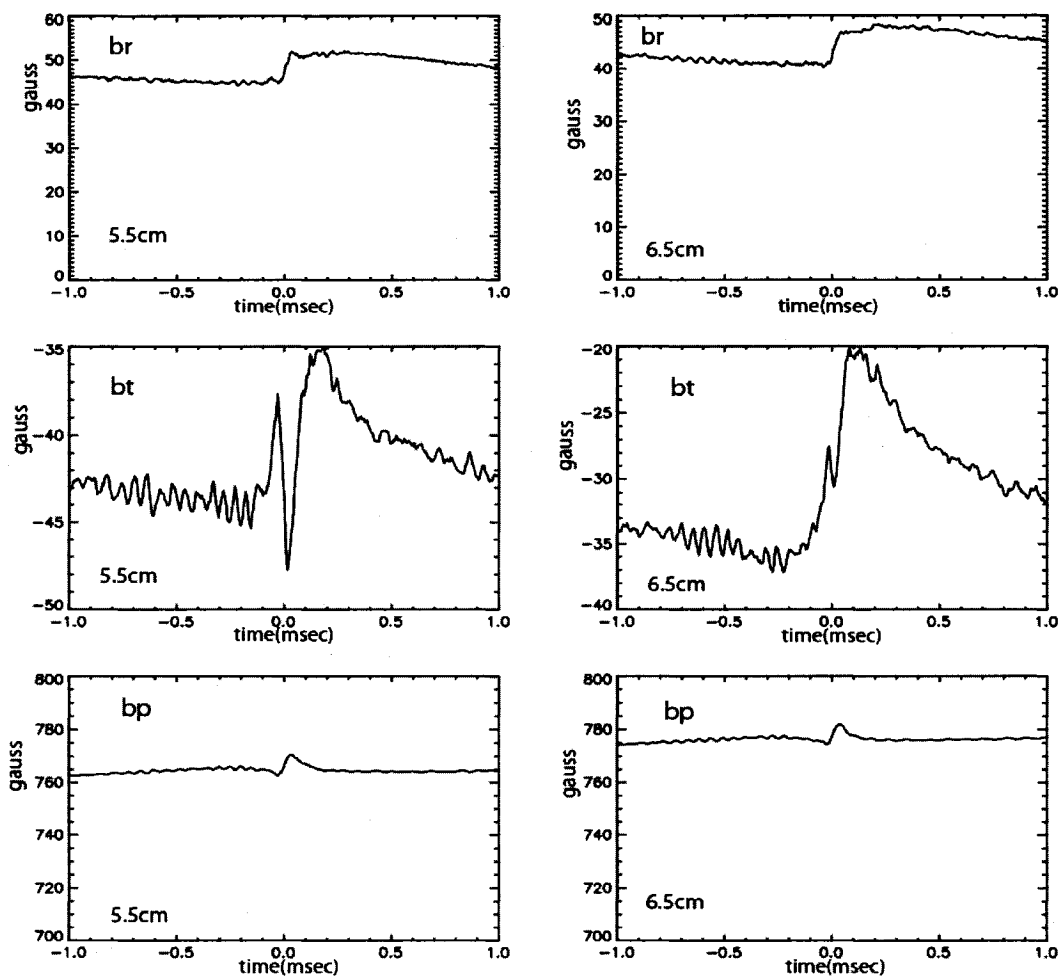


Figure 4.5 Equilibrium magnetic field quantities (br, bt, bp) during one sawtooth at radial depth 5.5cm and 6.5cm

Figure 4.6 shows the ensemble averaged magnetic fields during the EC burst. The toroidal magnetic field is more negative than for the sawtooth because the EC plasmas were more deeply reversed. This means the  $m=0$  resonant surface is located at a deeper radial point than for the sawtooth. The largest change during the burst is in the toroidal component which becomes more negative at both radii. This means the  $m=0$  resonant surface moves toward the center at the crash, in contrast to the sawtooth case.

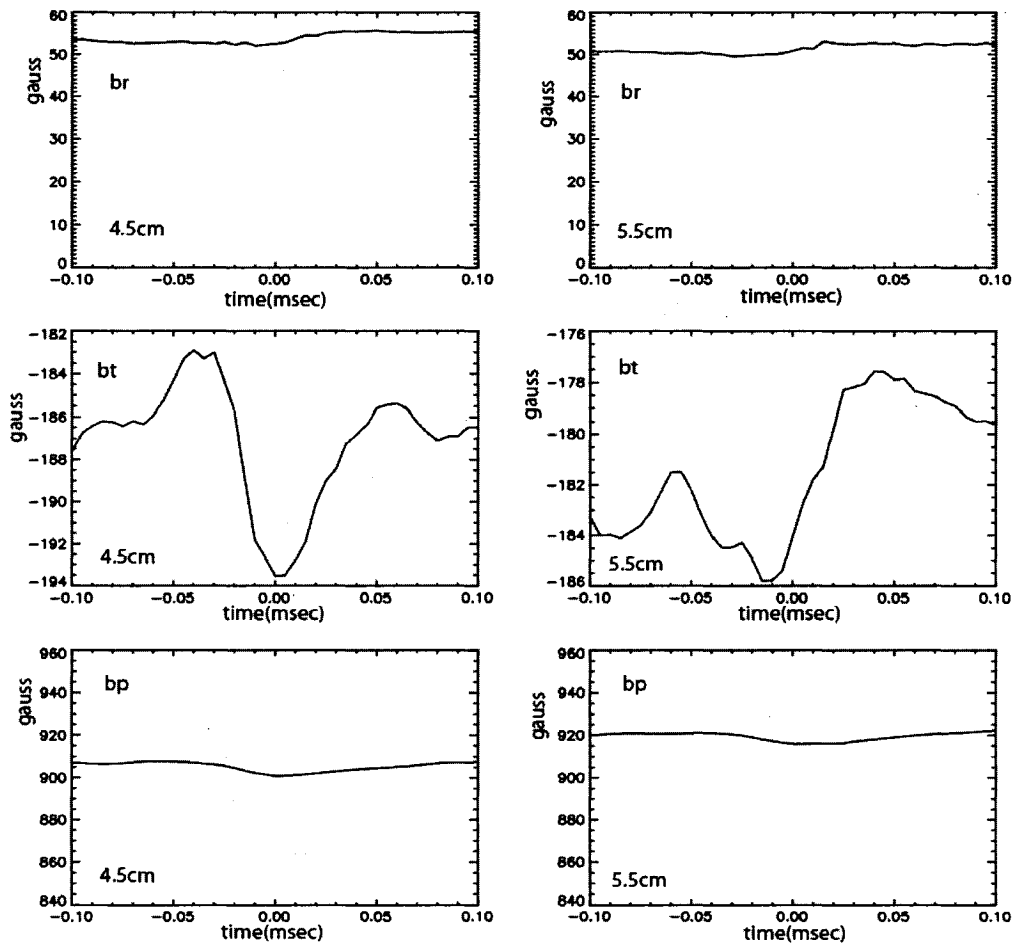


Figure 4.6 Equilibrium magnetic field quantities (br, bt, bp) during one EC burst at radial depth 5.5cm and 6.5cm

Figure 4.7 shows the ensemble averaged magnetic fields during QSH. The equilibrium magnetic fields are noisy during the period of mode growth in QSH. This fluctuation pattern is unique to QSH. The toroidal magnetic field has a value near zero because the QSH plasmas are obtained with  $F \sim 0$ . The  $m=0$  resonant surface is located at the vacuum vessel in this case.

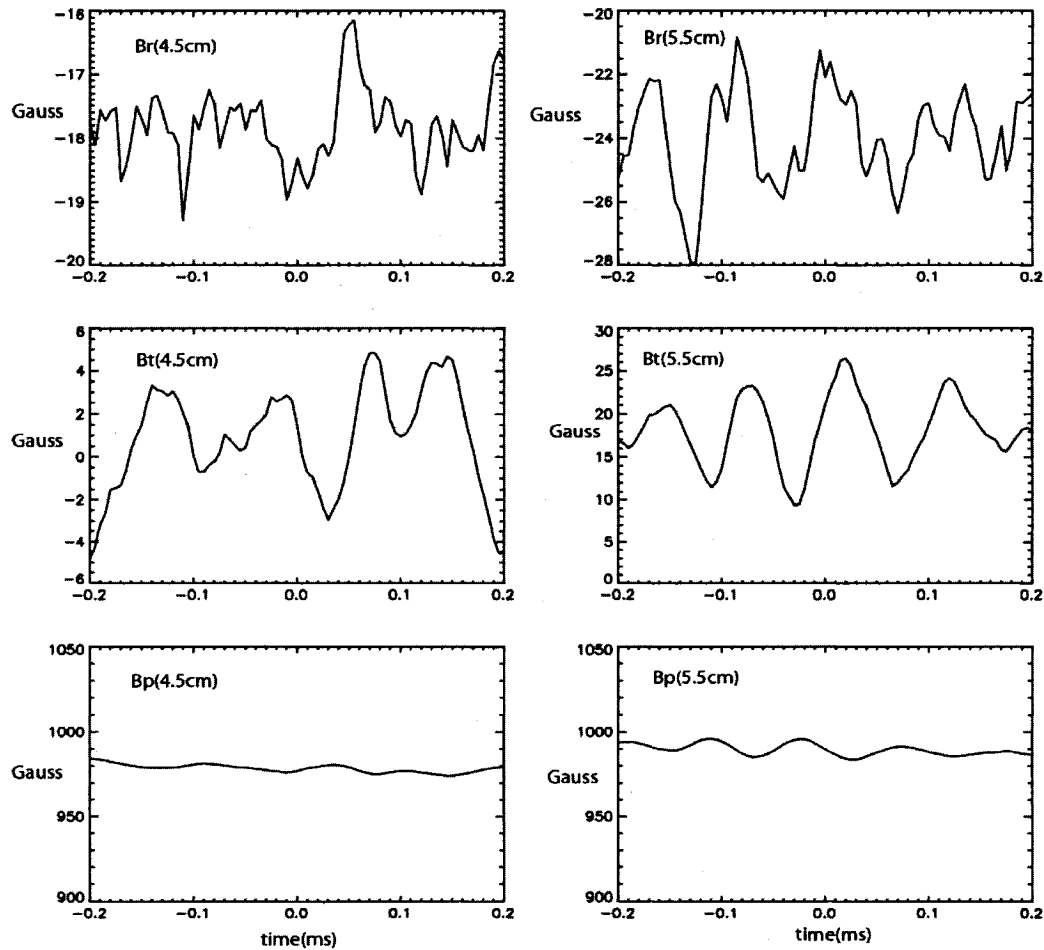


Figure 4.7 Equilibrium magnetic field quantities (br, bt, bp) during QSH at radial depth 5.5cm and 6.5cm

#### 4.4 Measurements of fluctuation quantities

##### Plasma potential and electric field fluctuations

The plasma potential is used to find the electric field at the edge of MST. This means that the radial, toroidal, and poloidal derivatives of the plasma potential fluctuations should be considered to get the electric field fluctuations. We use a cylindrical coordinate system with the  $z$  component replaced by  $R\phi$ . The modes of electric field are then given by

$$E_r^{m,n} = -\frac{\partial \Phi^{m,n}}{\partial r}$$

$$E_\theta^{m,n} = -\frac{1}{r} \frac{\partial \Phi^{m,n}}{\partial \theta} = -i \frac{m}{r} \Phi^{m,n} \quad (4.1)$$

$$E_\phi^{m,n} = -\frac{\partial \Phi^{m,n}}{\partial z} = -\frac{1}{R} \frac{\partial \Phi^{m,n}}{\partial \phi} = -i \frac{n}{R} \Phi^{m,n}$$

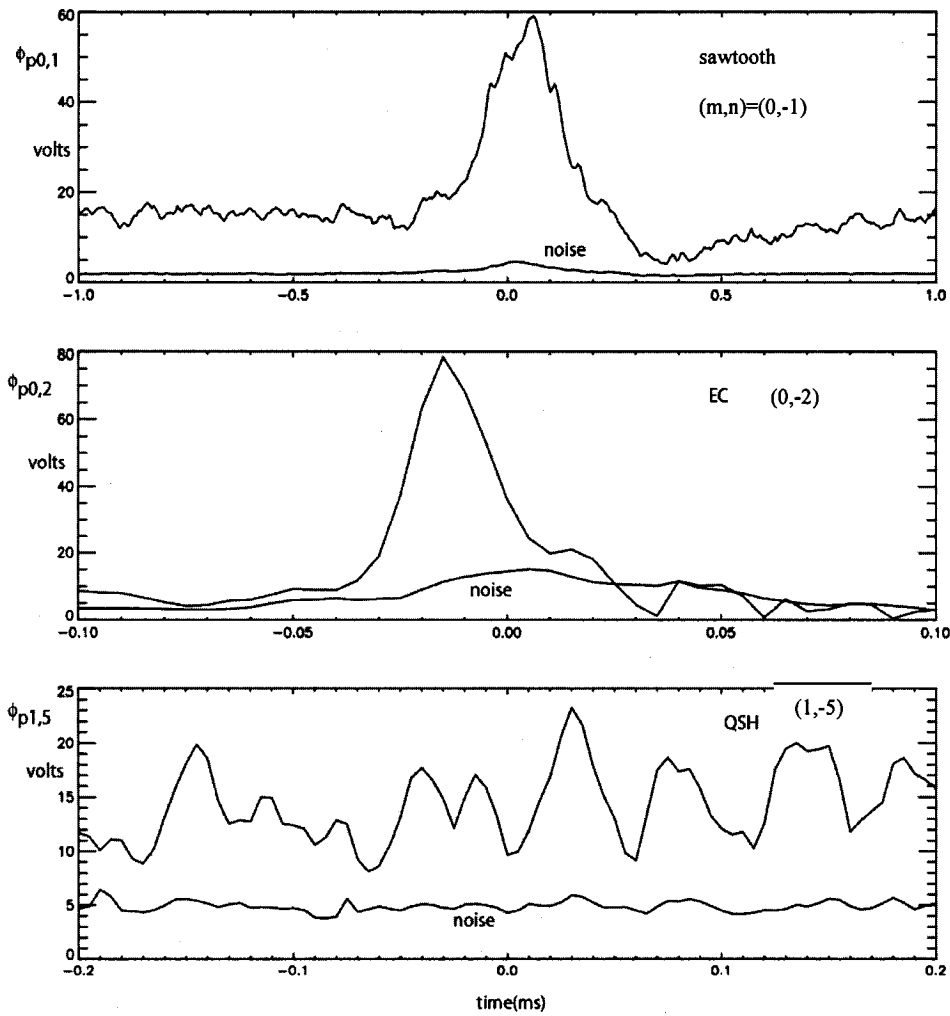


Figure 4.8 Mode amplitude of plasma potential ( $\Phi_p$ ) at 5.5cm in three different plasmas. The lower curve in each case is the statistical noise level.



The toroidal and the poloidal derivatives are derived from the  $e^{i(m\theta+n\phi)}$  dependence in the modes of plasma potential  $\Phi^{m,n}$ . The  $\Phi^{m,n}$  is derived by computing the correlation of the measured  $\Phi_p$  with a particular mode in the toroidal array of magnetic coils (described in chapter 3).

Figure 4.8 shows the ensemble averaged pseudo-spectral mode amplitudes of plasma potential in the three different plasma types. The poloidal mode number  $m = 0$ , toroidal mode number  $n = -1$  is shown for the sawtooth;  $m=0, n=-2$  for the EC; and  $m=1, n=-5$  for the QSH. The most dominant mode in each plasma is presented in figure 4.8. In chapter 3 it was noted that good mode rotation (uniform sampling of different mode phases) is needed to estimate the pseudo spectral fluctuation amplitudes. This condition is satisfied for each of the modes shown in figure 4.8. The  $(m,n)=(0,-1)$  mode in EC plasma has poor rotation but similar magnitude compared to the  $(0,-2)$  mode. Hence we use the  $(0,-2)$  mode for the pseudo-spectrum. The noise level for each case is the statistical error.

$$noise = \left( \frac{1}{N} \frac{\langle \Phi^2 a^2 \rangle}{\langle a^2 \rangle} \right)^{1/2},$$

where  $N$  is the ensemble size,  $\Phi$  is the total measured fluctuation level and  $a$  is the amplitude of the magnetic fluctuation from the toroidal array. From the measurement of plasma potential, the electric field is calculated.

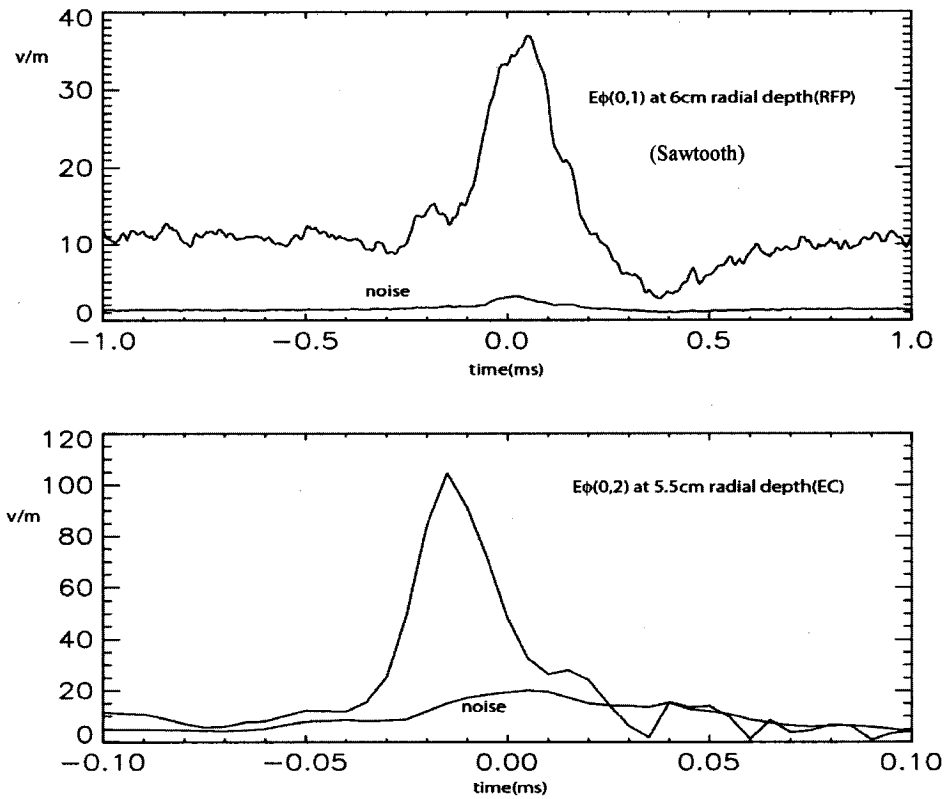


Figure 4.9  $m=0$  mode amplitudes of electric fields in sawtooth and EC plasmas

Figure 4.9 shows the ensemble averaged mode amplitudes of toroidal electrical field with  $m=0$ ,  $n=1$  for the sawtooth and  $m=0$ ,  $n=2$  for the EC plasma. They are measured at 6cm and 5.5cm in from the wall respectively. This is just outside the  $m=0$  resonant surface. The electric field is calculated from  $E_{\phi}^{0,n} = k_{\phi} \Phi^{0,n}$  and  $\Phi^{0,n}$  is the  $(0,n)$  mode of plasma potential. We can say that the toroidal electric field is excited near the burst time in both plasmas from figure 4.9. The toroidal electric field gives rise to the radial  $\vec{E} \times \vec{B}$  velocity which is the relevant quantity for MHD mode evolution equation for  $b_{\phi}^{0,n}$ .

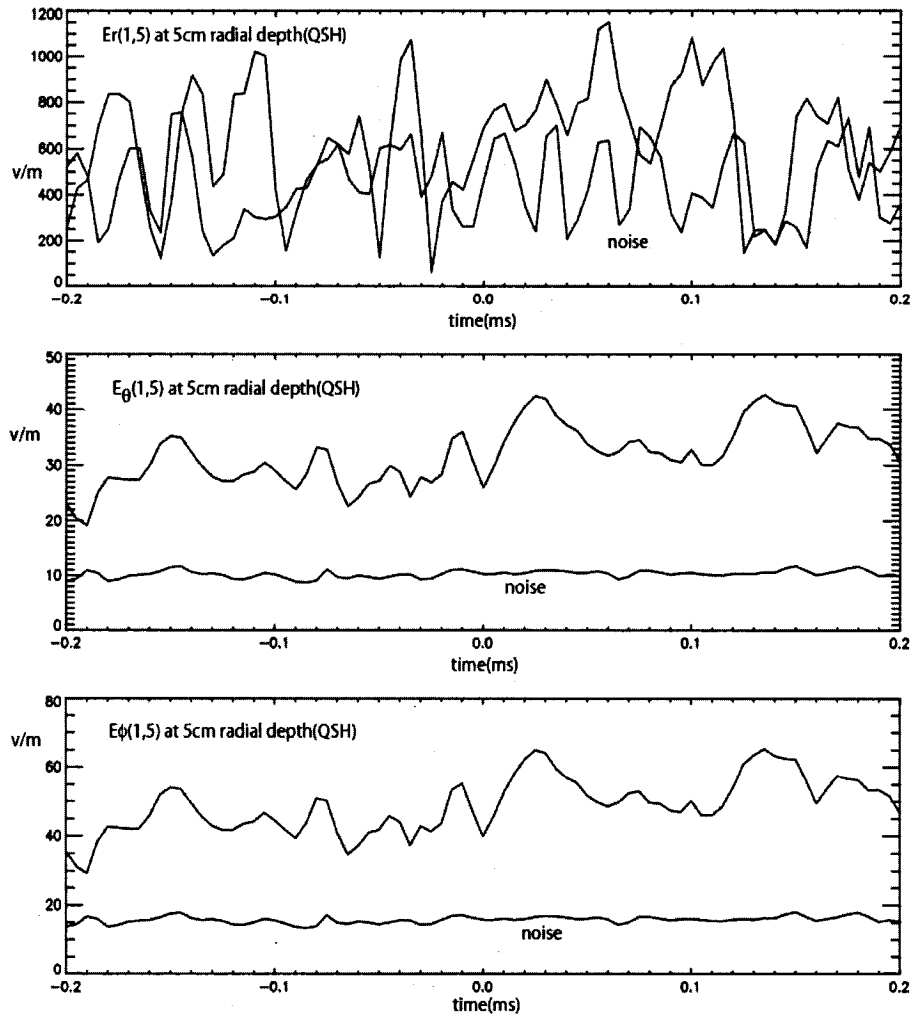


Figure 4.10  $m=1$  mode amplitudes of electric fields in QSH plasmas

Figure 4.10 shows the ensemble averaged mode amplitudes of electric field in three directions (radial, poloidal, toroidal) in QSH with  $m=1$ ,  $n=5$  at 5cm inside the wall. The radial component of electric field is the largest component and allows the largest noise level. The radial component is almost the same size as the noise level which, as we

will see in Chapter 5, makes it difficult to be certain of the sign of the mode driving terms in the QSH case. Here  $E_{\phi}^{1,5} = k_{\phi} \Phi^{1,5}$ ,  $E_{\theta}^{1,5} = k_{\theta} \Phi^{1,5}$ , and  $E_r^{1,5} = -\frac{\partial \Phi^{1,5}}{\partial r}$ . The radial derivative is calculated from the difference of measurements at 4.5cm and 5.5cm radial depth. The poloidal and the toroidal components are from the average of measurements at two radial points. Unlike the sawtooth and EC burst, QSH shows the slow variation during mode growing time.

### Velocity fluctuations

The velocity fluctuations are derived from the electric field fluctuations and the equilibrium magnetic fields. In order to measure the linear drive terms in the MHD equation, we need the component of velocity perpendicular to the magnetic field ( $v_{\perp}$ ). This velocity is dominantly the  $E \times B$  velocity. The electrostatic potential is dominant in MST. For example, the  $(m,n) = (0,-1)$  component of velocity is then given by

$$\vec{v}^{-0,-1} = \frac{1}{|B|^2} (\vec{E}^{-0,-1} \times \vec{B}^{-0,0}) + \frac{1}{|B|^2} (\vec{E}^{-0,0} \times \vec{B}^{-0,-1})$$

$$\vec{E}^{-0,-1} = -\vec{\nabla} \phi_p^{0,-1}$$

$$\vec{E}^{-0,0} = -\vec{\nabla} \phi_p^{0,0}$$

Figure 4.11 shows the radial velocity for  $m=0, n=-1$  for the sawtooth crashes and  $m=0, n=-2$  for the EC burst.

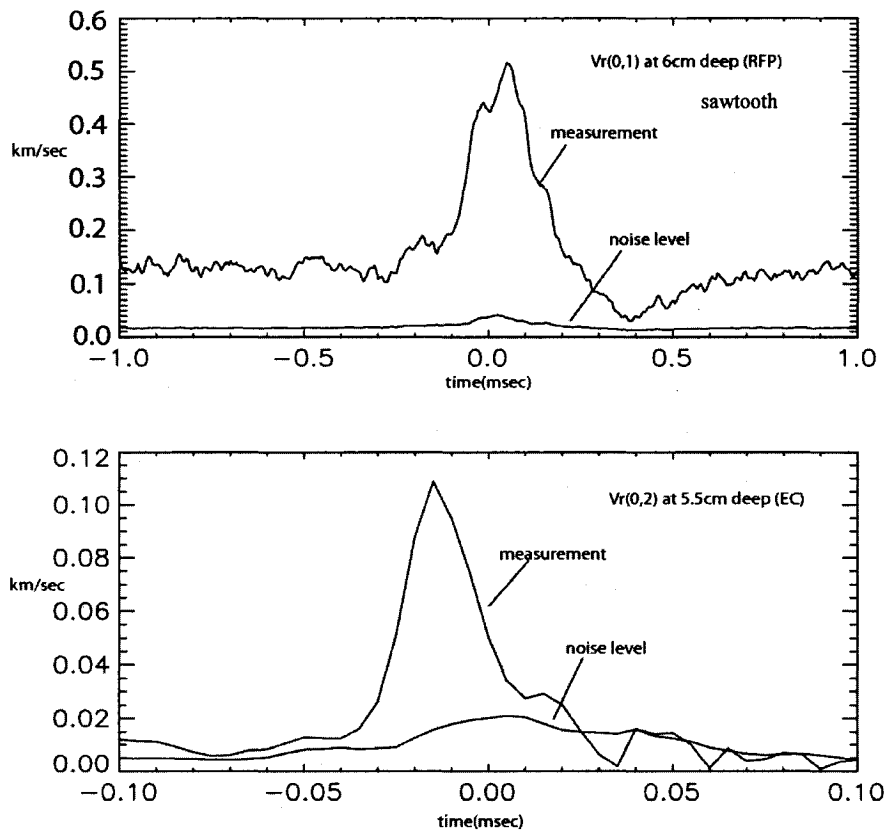


Figure 4.11  $m=0$  radial component of velocity fluctuation in sawtooth crash and EC burst

The radial location of measurement for the sawtooth crash is 6cm inside the MST wall and in EC plasma it is 5.5cm deep. The measured velocity fluctuation is well above the noise level during the burst in amplitude for both sawtooth and EC plasmas.

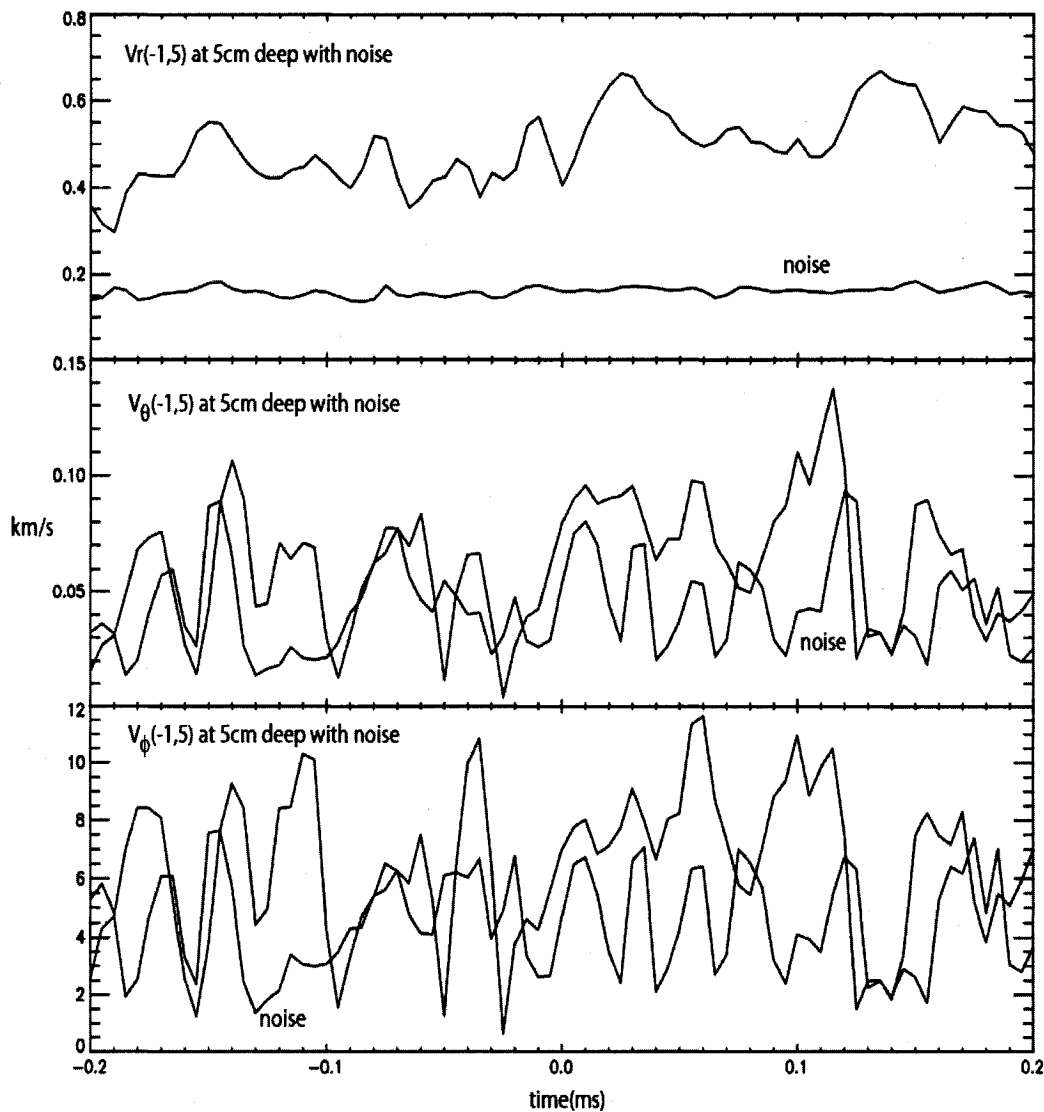


Figure 4.12  $m=1$  mode velocity fluctuations in QSH plasma

Figure 4.12 shows the velocity fluctuations with  $m=1$  and  $n=5$  in the QSH plasma. The radial location of measurement is 5cm deep. The toroidal component of velocity is dominant. The statistical error is comparable with the measured velocity for the poloidal and toroidal components. This comes from the error in the radial electric field (Fig. 4.10)

because the poloidal and toroidal velocity are derived from the radial electric field. The radial velocity is more reliably measured. The high noise level in poloidal and toroidal component will lead to uncertainty in the estimation of the linear term in the MHD equation for QSH plasmas.

### Magnetic fluctuations

Each component of magnetic field is measured with the b-dot probe at several radii. The magnetic field fluctuations are derived from these measurements by correlation with the Fourier coefficients of the toroidal array of edge coils. Figure 4.13 shows ensemble averaged  $m=0$  mode amplitude of the toroidal component of magnetic field for the sawtooth crash ( $n=-1$ ) and EC burst ( $n=-2$ ).

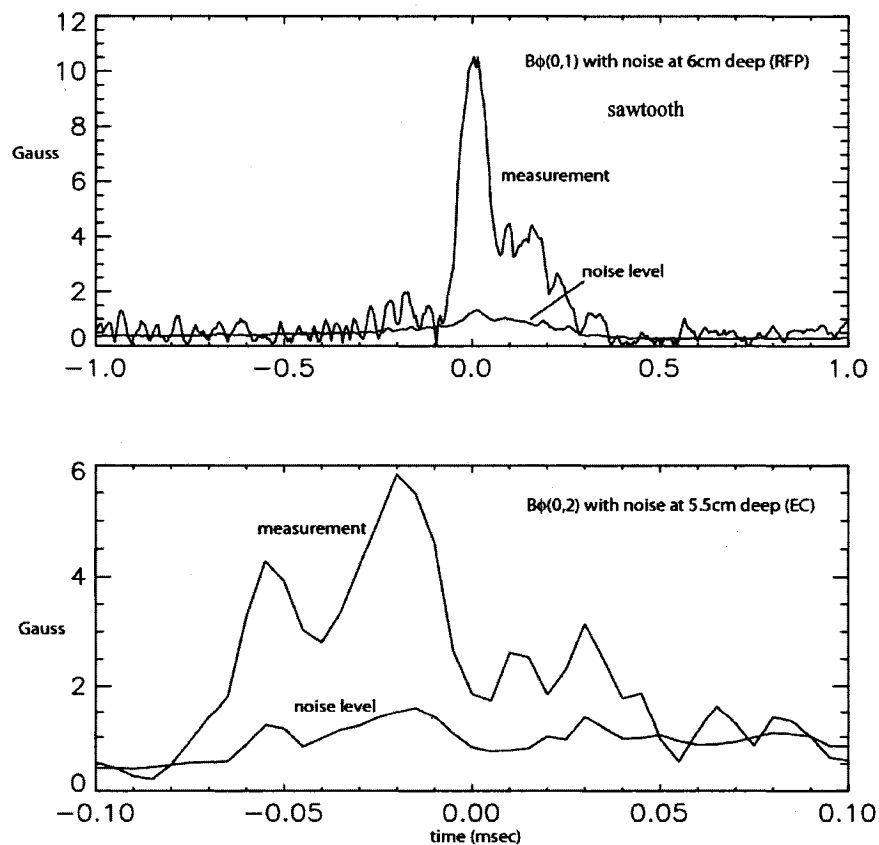


Figure 4.13  $m=0$  modes of toroidal magnetic field in sawtooth crash and EC burst

The radial locations of the measurements are 6cm and 5.5cm deep respectively. The amplitudes rise at the crash and burst above noise level.

Figure 4.14 shows the ensemble averaged radial, poloidal and toroidal magnetic field fluctuations with mode number  $m=1$  and  $n=5$  in QSH. The radial location of measurement is 5cm deep for these data. The measurement of magnetic field is well above the noise level unlike the potential and velocity (see Fig. 4.10 and 4.12). The radial component of magnetic field is small near the conducting boundary of MST. The oscillation in fluctuation amplitudes in figure 4.14 are due to errors in the measurements and finite ensemble size.

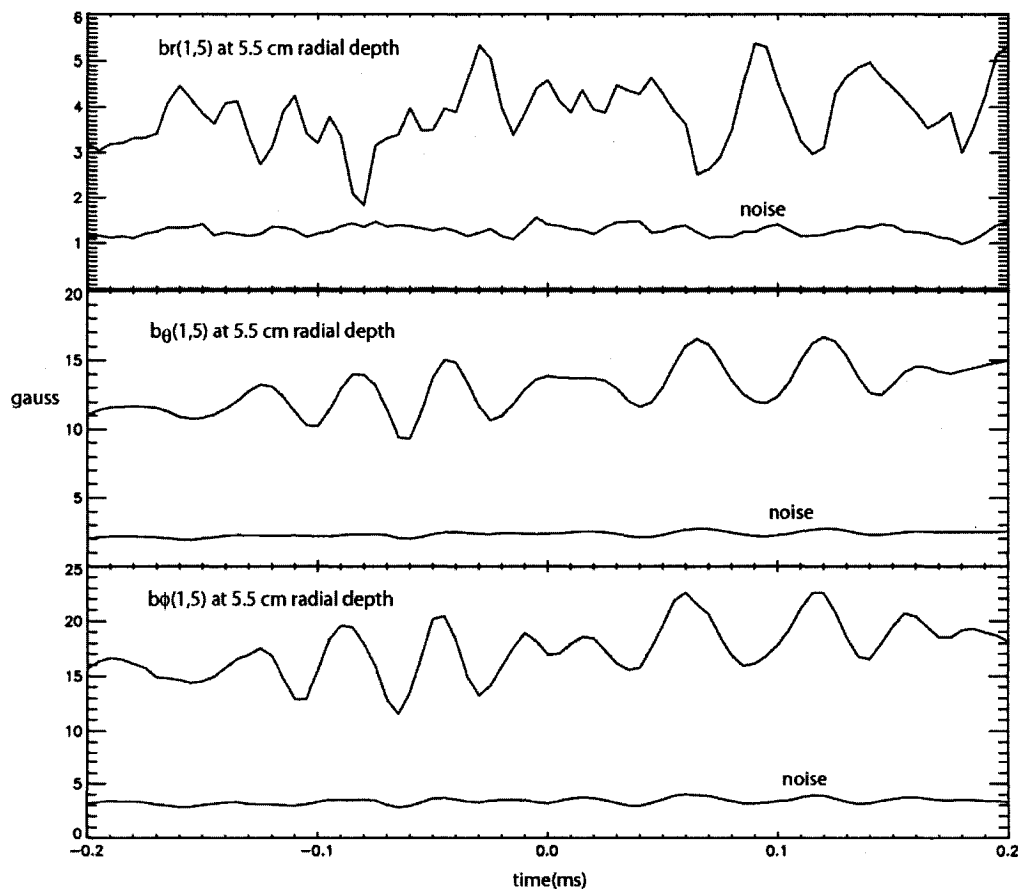


Figure 4.14  $m=1$  modes of magnetic field in QSH plasma



## 5. Stability of $m=0$ and $m=1$ modes

### 5.1 Introduction

In this chapter, we investigate the energy flow between modes using the pseudo-spectrum measurements of velocity and magnetic field fluctuations described in chapter 4. We focus on the modes with poloidal mode number  $m=0$  and toroidal mode numbers  $n=1$  in sawtooth crash and the  $n=2$  bursts in EC. We also examine the  $m=1, n=5$  in the QSH plasma where it is the dominant mode. The energy equation for magnetic fluctuations is considered to find whether each mode is stable. The linear terms in the magnetic field energy equation are measured and the sign of the measured quantity will determine if the mode is stable or unstable. A negative sign means stable and a positive sign means unstable. We also examine the nonlinear terms which describe the energy flow between modes.

From Maxwell's equations and the simple form of resistive Ohm's law, we can find the magnetic induction equation.

$$\begin{aligned}
 \vec{E} + \vec{v} \times \vec{B} &= \eta \vec{J} \\
 \nabla \times \vec{E} &= \frac{\partial \vec{B}}{\partial t} \\
 \nabla \times \vec{B} &= \mu_0 \vec{J} \\
 \rightarrow \frac{\partial \vec{B}}{\partial t} &= \nabla \times (\vec{v} \times \vec{B}) + \frac{\eta}{\mu_0} \nabla^2 \vec{B}
 \end{aligned} \tag{5.1}$$

The Hall effect can be important in Ohm's law near resonant surfaces but is measured to be small in the region of our measurements[1,2]. The second term ( $\frac{\eta}{\mu_0} \nabla^2 \vec{B}$ ) on the right hand side of the magnetic induction equation represents resistive dissipation and is very

small near the edge of MST where our measurements are made. Breaking equation 5.1 into the Fourier modes we obtain (neglecting resistive dissipation)

$$\begin{aligned}\vec{B}(r, \vartheta, \phi, t) &= \sum_{m,n} \vec{b}_{m,n}(r, t) \exp(im\vartheta + in\phi) \\ \frac{\partial \vec{b}_{i,j}}{\partial t} &= \nabla \times (\vec{v}_{i,j} \times \vec{b}_{0,0}) + \nabla \times (\vec{v}_{0,0} \times \vec{b}_{i,j}) + \sum_{\substack{i=l+m \\ j=p+q}} \nabla \times (\vec{v}_{l,p} \times \vec{b}_{m,q})\end{aligned}\quad (5.2)$$

The first two terms  $[\nabla \times (\vec{v}_{i,j} \times \vec{b}_{0,0}) + \nabla \times (\vec{v}_{0,0} \times \vec{b}_{i,j})]$  in equation 5.2 are linear terms and the last terms  $[\sum_{\substack{i=l+m \\ j=p+q}} \nabla \times (\vec{v}_{l,p} \times \vec{b}_{m,q})]$  are nonlinear terms. We use a cylindrical coordinate system [3]. From equation 5.2, we obtain the magnetic energy equation:

$$\frac{\partial |\vec{b}_{i,j}|^2}{\partial t} = \left\{ \nabla \times (\vec{v}_{i,j} \times \vec{b}_{0,0}) + \nabla \times (\vec{v}_{0,0} \times \vec{b}_{i,j}) + \sum_{\substack{i=l+m \\ j=p+q}} \nabla \times (\vec{v}_{l,p} \times \vec{b}_{m,q}) \right\} \cdot \vec{b}_{i,j}^* + C.C \quad (5.3)$$

The complex conjugate term insures that the energy is a purely real quantity. In the following sections, we combine the measured pseudo-spectral quantities from chapter 4 to derive the terms in equation 5.3 for the different plasma types. We assume that the sign of the linear term is independent of radius. In linear theory this is true. The nonlinear computational results show that the sign of the radial integration of the linear term and the linear term at a specific edge radial point for the  $m=0, n=1$  mode are the same. If the sign were different at different radii, it would imply that the source of mode energy is different at different radii. This seems unlikely but cannot be strictly ruled out without making more measurements beyond the range where our probes can operate.

## 5.2 Stability of $m=0$ mode in the sawtooth

For the  $m=0$   $n=1$  mode, the magnetic energy equation for the toroidal component, keeping only the first linear term is;

$$\begin{aligned} \frac{\partial |b_{\phi}^{0,-1}|^2}{\partial t} &= \nabla \times (\vec{v}^{0,-1} \times \vec{b}^{0,0})_{\phi} \cdot b_{\phi}^{0,-1*} + C.C \\ &= -\frac{1}{r} (v_r^{0,-1} b_{\phi}^{0,0} b_{\phi}^{0,-1*}) - \left( \frac{\partial}{\partial r} v_r^{0,-1} \right) b_{\phi}^{0,0} b_{\phi}^{0,-1*} - v_r^{0,-1} \left( \frac{\partial}{\partial r} b_{\phi}^{0,0} \right) b_{\phi}^{0,-1*} + C.C \end{aligned} \quad (5.4)$$

We have evaluated the second linear term in equation 5.3 for this case and found it to be small. Each individual term on the right side of equation 5.4 is measured directly and added together to infer the stability of the  $m=0$ ,  $n=1$  mode. Figure 5.1 (a) shows the  $m=0$  linear term (right hand side of equation 5.4). The error bars show the variation possible given the finite ensemble size and associated error in the correlations. Figure 5.1 (b) shows the time derivative of magnetic field energy (left side of equation 5.4).

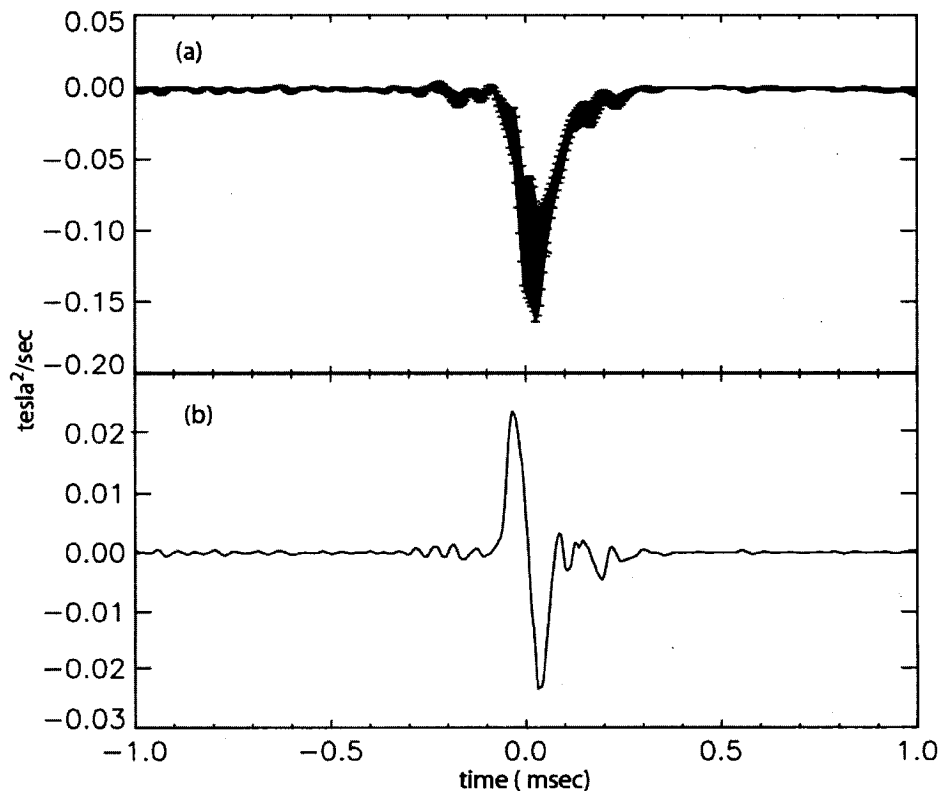


Fig 5.1 (a)  $m=0$  linear term and (b) time derivative of magnetic energy (left side of Eq 5.3)

The  $m=0$  linear term is negative during the sawtooth crash. This means that the  $m=0$  mode is stable during the entire sawtooth crash. The negative sign means that the energy goes from the  $m=0, n=1$  mode to the  $m=0, n=0$  equilibrium. Hence we can say the equilibrium field gains energy from the  $m=0$  mode during the entire sawtooth crash. Hence, the sudden growth of the mode at the sawtooth crash does not occur due to instability. The energy source must be from either other modes or effects not described by the MHD equations we are considering here.

### 5.3 Comparison with MHD computation

As pointed out previously, the RFP sawtooth cycle has been studied for many years and MHD computation has been a very useful tool for understanding the behavior of the different modes [4]. The DEBS code is a 3D, nonlinear resistive MHD code that solves the nonlinear, resistive MHD equations in cylindrical geometry [5]. It uses a finite difference method in the radial direction and fast Fourier transform in the poloidal and toroidal directions. The simulation has been used to estimate the same linear term of equation 5.3 and the result also shows the stability of  $m=0$  modes during the crash (fig 5.2). The linear term is negative during the entire crash phase in computation. The result from direct measurement and the result from DEBS code are in good agreement (fig 5.1.a and fig 5.2). The DEBS simulation is done in a parameter regime (Lundquist number and radial location) similar to the real measurement. In the computation, the growth of the  $m=0$  mode is due to nonlinear coupling of core resonant  $m=1$  modes. In the next section we examine this in MST.

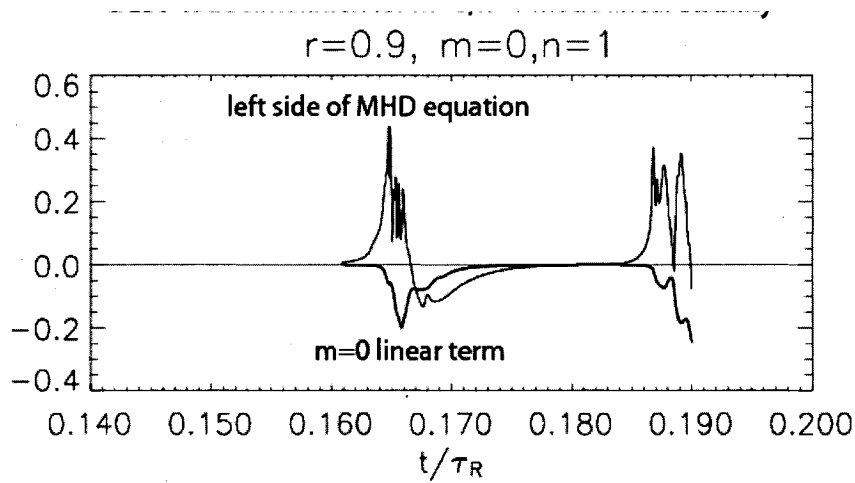


Fig 5.2 Computation result (DEBS code) of  $m=0$  linear term [6]

#### 5.4 Nonlinear stability of $m=0$ mode in sawtooth

The bi-spectrum between  $m=0$  and  $m=1$  modes at the edge of MST shows that there is nonlinear coupling between these modes (see section 3.4). It indicates that coupling exists but does not give the direction of energy flow. So the  $m=1$ ,  $n=-5,-6,-7,-8,-9,-10$  modes have been measured to explore the nonlinear energy flow from  $m=1$  modes to  $m=0$  modes during the sawtooth crash. The  $m=0$  mode evolution, keeping only the nonlinear drive term is

$$\begin{aligned}
 \frac{\partial b_{\phi}^{0,-1}}{\partial t} &= \nabla \times (\tilde{v} \times \tilde{b})_{\phi} \\
 \frac{\partial b_{\phi}^{0,-1}}{\partial t} &= \sum_{n=6}^{10} \frac{1}{r} (v_{\phi}^{1,n} b_r^{1,n+1*} - v_r^{1,n} b_{\phi}^{1,n+1*}) + \frac{\partial}{\partial r} (v_{\phi}^{1,n} b_r^{1,n+1*} - v_r^{1,n} b_{\phi}^{1,n+1*}) \\
 &\dots\dots\dots + \frac{1}{r} (v_{\phi}^{1,n+1*} b_r^{1,n} - v_r^{1,n+1*} b_{\phi}^{1,n}) + \frac{\partial}{\partial r} (v_{\phi}^{1,n+1*} b_r^{1,n} - v_r^{1,n+1*} b_{\phi}^{1,n})
 \end{aligned} \tag{5.5}$$

The measurement of nonlinear terms includes many more terms than linear measurement.

Converting equation 5.5 to an energy equation, we find

$$\begin{aligned}
\frac{\partial |b_{\phi}^{0,-1}|^2}{\partial t} &= \sum_{n=6}^{10} \frac{1}{r} (v_{\phi}^{1,n} b_r^{1,n+1*} - v_r^{1,n} b_{\phi}^{1,n+1*}) \times b_{\phi}^{0,-1*} \\
&+ \frac{\partial}{\partial r} (v_{\phi}^{1,n} b_r^{1,n+1*} - v_r^{1,n} b_{\phi}^{1,n+1*}) \times b_{\phi}^{0,-1*} \\
&+ \frac{1}{r} (v_{\phi}^{1,n+1*} b_r^{1,n} - v_r^{1,n+1*} b_{\phi}^{1,n}) \times b_{\phi}^{0,-1*} \\
&+ \frac{\partial}{\partial r} (v_{\phi}^{1,n+1*} b_r^{1,n} - v_r^{1,n+1*} b_{\phi}^{1,n}) \times b_{\phi}^{0,-1*} \\
&+ \text{Complex..Conjugate}
\end{aligned} \tag{5.6}$$

Figure 5.3 (a) shows the  $m=0$  nonlinear terms (right side of equation 5.6) with noise level and the figure 5.3 (b) shows the time derivative of magnetic field energy (left side of equation 5.6). For the nonlinear measurement,  $n=5$  and  $n=6$  are chosen in equation 5.6 because they are the dominant modes. A positive sign at the sawtooth crash would mean that the  $m=0$  mode is nonlinearly driven through the nonlinear coupling between  $m=1$  modes. However, the noise level is too large to confidently assign a positive or negative sign to the term. The main reasons that the measurement of the nonlinear term is not resolved are

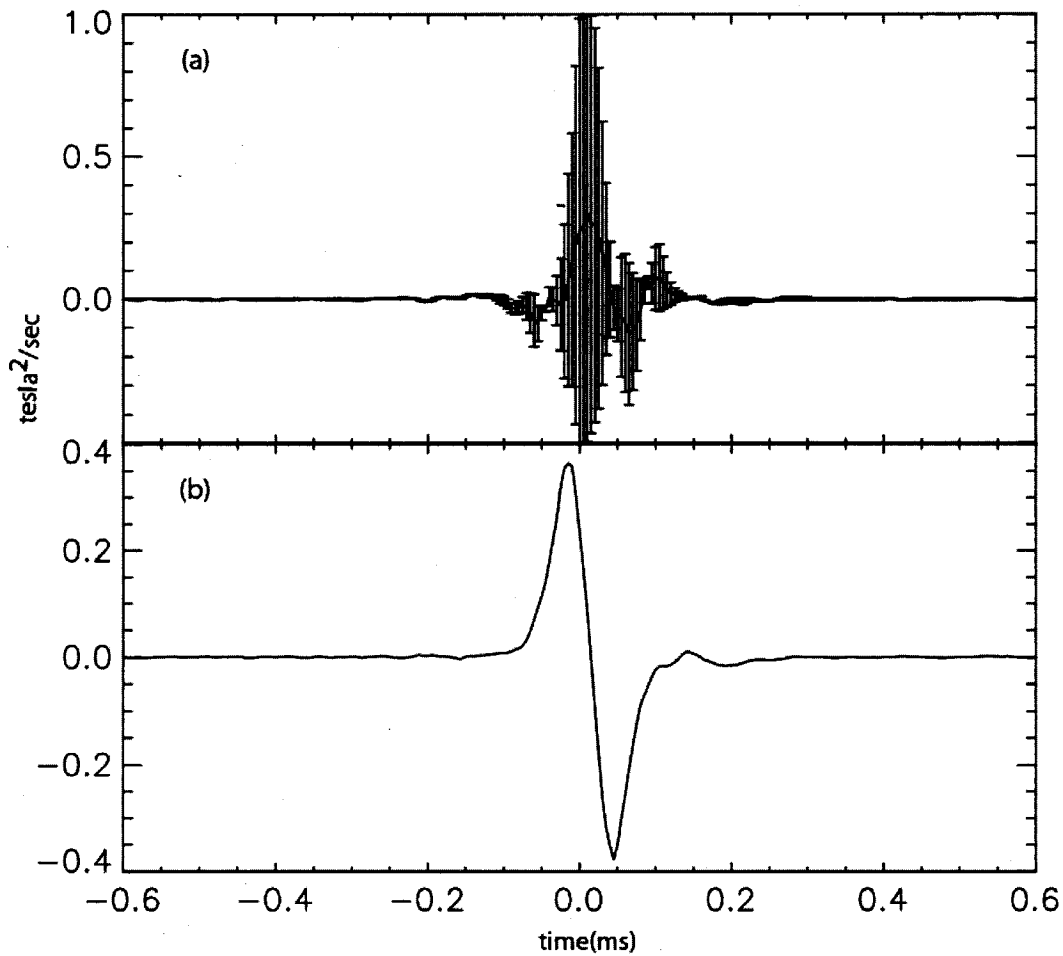


Fig 5.3  $m=0$  nonlinear term (a) and time derivative of magnetic energy (b)

1. Nonlinear term measurement requires many more terms than the linear drive measurement, and hence the final result is more prone to error.
2. The  $m=0$  modes are strong in the measured signals (potential and magnetic fields) in the edge near the  $m=0$  resonant surface making the  $m=1$  modes more difficult to detect.
3. The  $m=1$  mode velocity fluctuations are small in the edge.

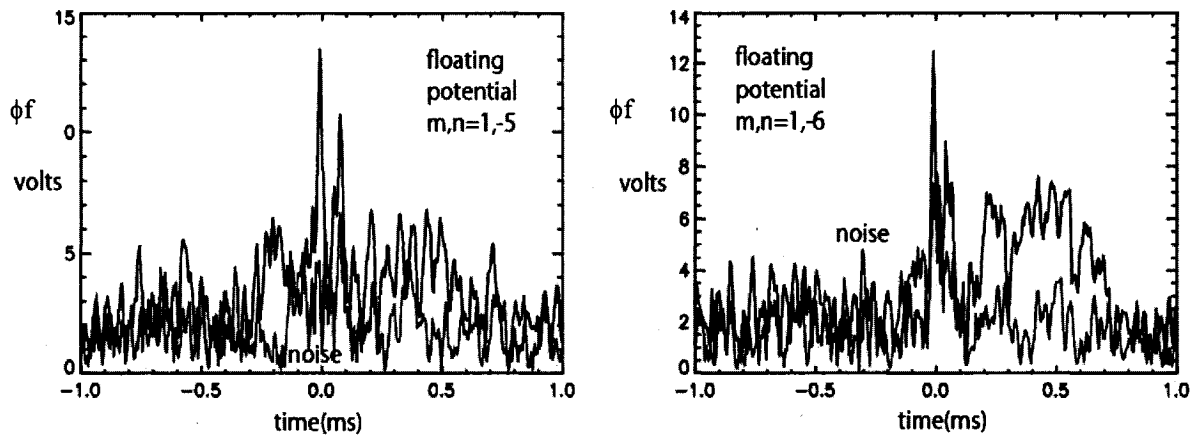


Fig 5.4 Magnitude of dominant modes in floating potential at 6.5cm radial depth

In figure 5.4, we show the pseudo-spectra for the  $m=1$  floating potential used in the calculation. The noise level is large and a strange bump after the sawtooth crash is present. The large bump is coming from the slow rotation of the modes and is very critical in applying the pseudo-spectrum method. Fast mode rotation is necessary to get the reliable data using the pseudo-spectrum. Although the nonlinear term is not resolved, the measurement of  $m=0$  stability coupled with a large bi-spectrum between  $m=0$  and  $m=1$  modes strongly suggests the  $m=0$  is driven nonlinearly, as expected from MHD computation.

### 5.5 Linear terms for $m=0$ mode in EC

In the bursts of  $m=0$  activity during EC periods, many  $n$ 's are excited. We focus on the  $m=0, n=-2$  because it is large and rotates well. The  $m=0, n=-1$  also increases at the burst but the slow mode rotation results in deformation of the shape of pseudo-spectrum (see the bump after  $t=0$  in Fig. 5.5 a).



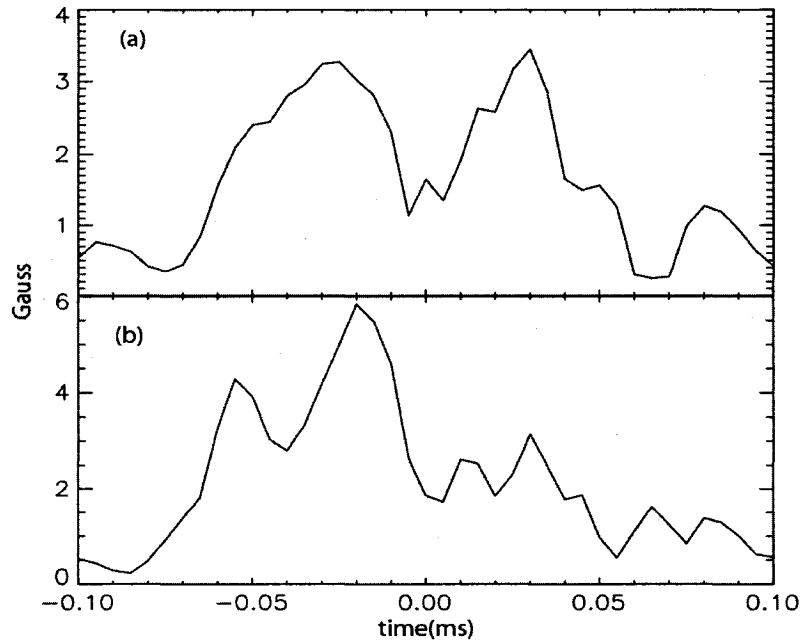


Fig 5.5 Magnitude of toroidal component of magnetic mode with  $m=0, n=-1$  (a) and  $m=0, n=-2$  (b)

The MHD equation for the toroidal component of the  $m=0, n=-2$  mode is;

$$\frac{\partial b_t^{0,-2}}{\partial t} = \nabla \times (\vec{v}^{-0,-2} \times \vec{b}^{0,0})_t$$

$$\frac{\partial |b_t^{0,-2}|^2}{\partial t} = -\frac{1}{r} (v_r^{0,-2} b_t^{0,0} b_t^{0,-2*}) - \left( \frac{\partial}{\partial r} v_r^{0,-2} \right) b_t^{0,0} b_t^{0,-2*} - v_r^{0,-2} \left( \frac{\partial}{\partial r} b_t^{0,0} \right) b_t^{0,-2*} \quad (5.7)$$

+ *Complex..Conjugate*

Each individual term in the right side of equation 5.7 is measured directly and adds up for stability of  $m=0$  and  $n=2$  mode.

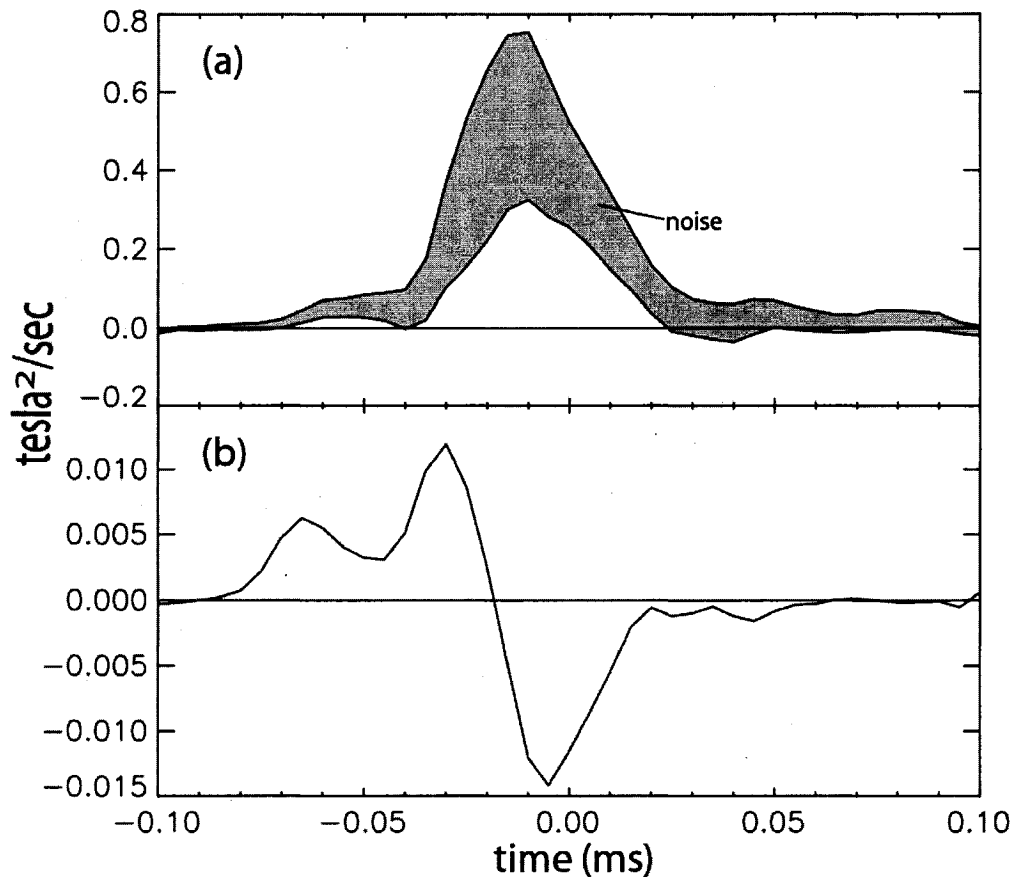


Fig 5.6  $m=0$  linear term (a) and time derivative of magnetic energy (b)

Figure 5.6 (a) shows the linear term for the  $m=0, n=-2$  mode (right side of equation 5.7) with noise level and figure 5.6 (b) shows the time derivative of magnetic field energy (left side of equation 5.7). Figure 5.6 (a) is positive and this means that the  $m=0$  mode in the EC burst is linearly unstable. We might also say that the energy goes from the equilibrium fields to  $m=0, n=-2$  mode because of the positive sign of the linear term during the  $m=0$  burst in EC. This result contrasts with sawtooth crash. Recall that one difference is that the  $m=0$  mode alone is excited in the EC burst (see figure 5.7). Hence, it

is reasonable to think that it might be unstable. This type of event has not yet been observed in MHD computation.

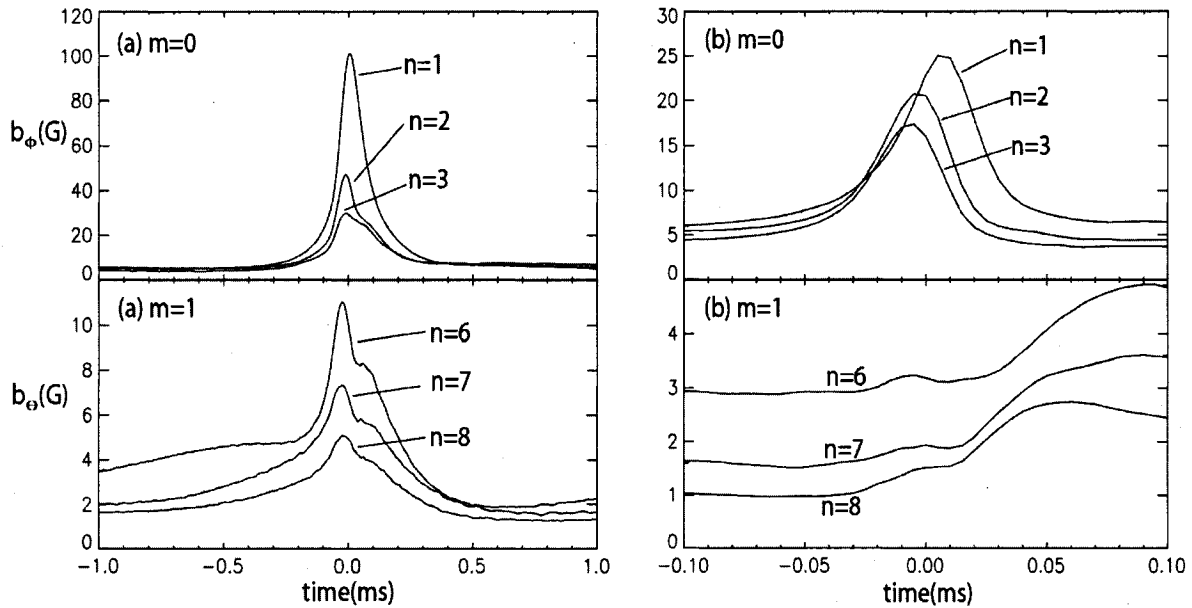


Fig 5.7 Contrast in  $m=0,1$  mode excitation between sawtooth crash (a) and EC burst (b)

### 5.6 Linear terms for $m=1$ mode in QSH

The  $m=1, n=-5$  is the dominant mode in the QSH plasmas examined in this thesis. The  $m=1, n=-5$  mode is appears in each component, poloidal and toroidal. Hence, we can examine the stability for each component. The MHD equation for the poloidal component of the  $m=1, n=-5$  mode is;

$$\frac{\partial b_g^{1,-5}}{\partial t} = \nabla \times (\vec{v}^{1,-5} \times \vec{b}^{0,0})_g$$

$$\frac{\partial |b_g^{1,-5}|^2}{\partial t} = -\frac{\partial}{\partial r} (v_r^{1,-5} b_g^{0,0}) \cdot b_g^{1,-5*} - \frac{1}{R} \frac{\partial}{\partial \phi} (v_\phi^{1,-5} b_g^{0,0} - v_g^{1,-5} b_\phi^{0,0}) \cdot b_g^{1,-5*} \quad (5.8)$$

+ *Complex..Conjugate*

Each individual term in right side of equation 5.8 is measured directly and added up to obtain the stability of the poloidal component of the m=1 and n=-5 mode. The MHD equation for the toroidal component of the m=1, n=-5 mode is;

$$\frac{\partial b_\phi^{1,-5}}{\partial t} = \nabla \times (\vec{v}^{1,-5} \times \vec{b}^{0,0})_\phi$$

$$\frac{\partial |b_\phi^{1,-5}|^2}{\partial t} = -\frac{1}{r} \frac{\partial}{\partial r} (r v_r^{1,-5} b_\phi^{0,0}) \cdot b_\phi^{1,-5*} + \frac{1}{r} \frac{\partial}{\partial \theta} (v_\phi^{1,-5} b_g^{0,0} - v_g^{1,-5} b_\phi^{0,0}) \cdot b_\phi^{1,-5*} \quad (5.9)$$

+ *Complex..Conjugate*

Each individual term in right side of equation 5.9 is also measured directly and added up to obtain the stability of the toroidal component of the m=1 and n=-5 mode. Figure 5.8 (a) shows the linear term for the poloidal component of the m=1 mode (right side of the first equation in equation 5.8) and figure 5.8 (b) shows the linear term for the toroidal component of the m=1 mode (right side of the second equation in equation 5.9). The linear term fluctuates during time because of a coherent noise in the toroidal array signals during QSH which is not fully understood. The linear drive term for the m=1 mode in the poloidal component is very weak and mostly negative (fig 5.8a). The linear drive term for the m=1 mode in the toroidal component is strong and mostly positive (fig 5.8b). Both

components are noisy due to the uncertainty in the radial electric field fluctuation as discussed in section 4.4. Because of the large noise, we cannot determine with certainty the sign of the linear term for either component and the result for the QSH case is inconclusive. In fact the measurement is more difficult in this case anyway because the mode growth is very slow in time.

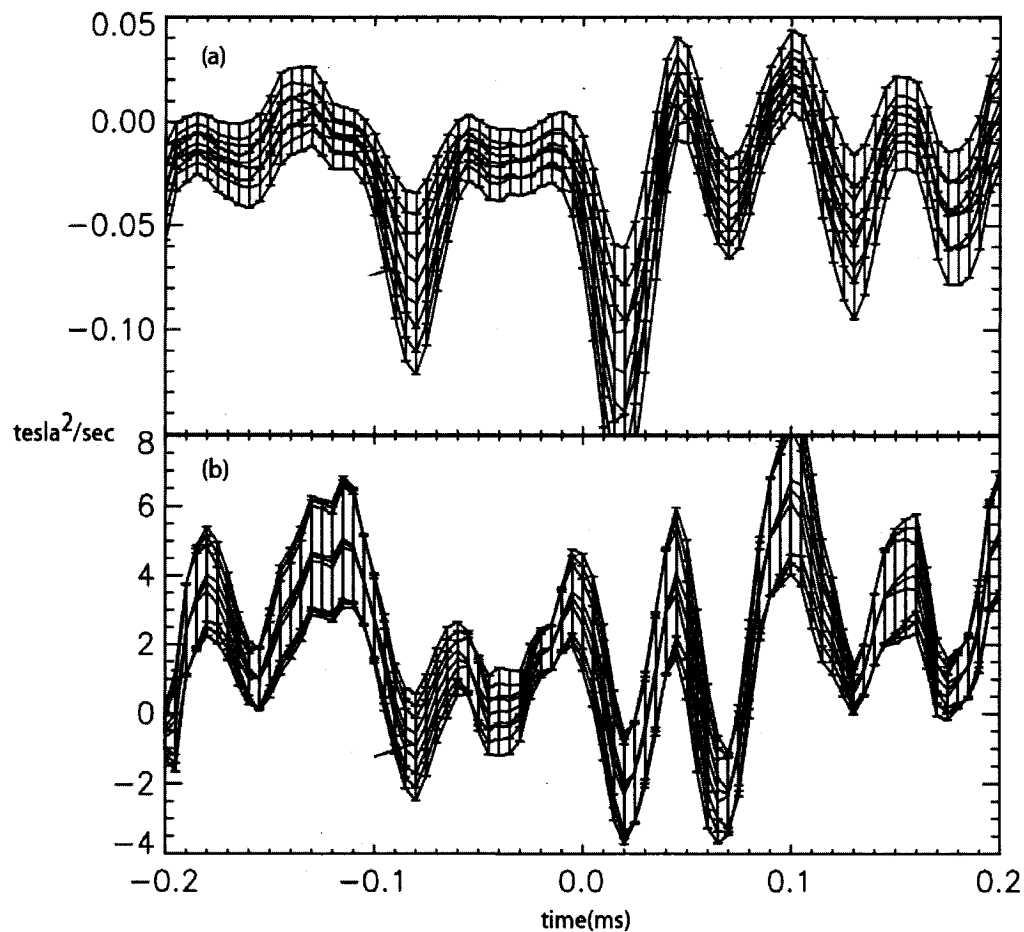


Fig 5.8  $m=1$  linear term in poloidal component (a) and  $m=0$  linear term in toroidal component (b)

## 5.7 Summary

We have determined the cause for reconnection in a laboratory plasma by measuring the term in MHD which accounts for the energy exchange between a magnetic fluctuation and the axisymmetric field. The measurement was made for three types of reconnection

events in the RFP: the normal sawtooth crash, enhanced confinement  $m=0$  burst, and slow growth quasi-single helicity. With sawtooth crash, the term is negative for modes with  $m=0$ , indicating that energy flows from the mode to the axisymmetric fields. A significant measured bi-spectrum between the  $m=0$  and  $m=1$  modes indicates that nonlinear coupling is present. This supports the standard picture that  $m=0$  modes are stable, but  $m=0$  reconnection is driven by nonlinear coupling to other modes [7]. In the EC  $m=0$  bursts, an opposite picture holds:  $m=0$  modes derive energy from the axisymmetric fields indicating they are unstable, corresponding to spontaneous reconnection. Such a picture awaits theoretical study and more complete equilibrium profile measurements. In the slow growth QSH plasmas, the term for the  $m=1$  mode in the poloidal component is very weak and mostly negative and for the toroidal component is strong and mostly positive. Because of the large noise, we cannot determine with certainty the sign of the linear term for either component and the result for the QSH case is inconclusive. These results support the possibility that nonlinear mode coupling could be important in reconnection in other laboratory and astrophysical venues. These techniques might also be useful to examine and understand how these modes are produced and may lead to improved ways to control them. For example, to control  $m=0$  modes in the normal sawtooth plasmas (the most dominant fluctuation in normal sawtooth plasmas), it appears one needs to control the  $m=1$  modes which cause them. However in improved confinement (EC) plasmas, where  $m=1$  modes are already suppressed, the  $m=0$  bursts should be controlled by the edge current or pressure profiles which affect the equilibrium fields since they are unstable.

**References**

1. W.X. Ding et al., Phys. Rev. Lett. **93**, 045002 (2004)
2. P.W. Fontana et al., Phys. Rev. Lett. **85**, 566 (2000)
3. Jeffrey P. Freidberg, Ideal Magneto Hydro Dynamics, Plenum press (1987)
4. Y. L. Ho, G. G. Craddock, Physics of Fluids B vol 3 pp721-734 (1990)
5. D.D Schnack et al., J. Comput. Phys. **70**, 330 (1987)
6. F. Ebrahimi, private communication (2005)
7. S. Choi et al., Phys. Rev. Lett. **96**, 145004 (2006)

### **Appendix ; Error analysis**

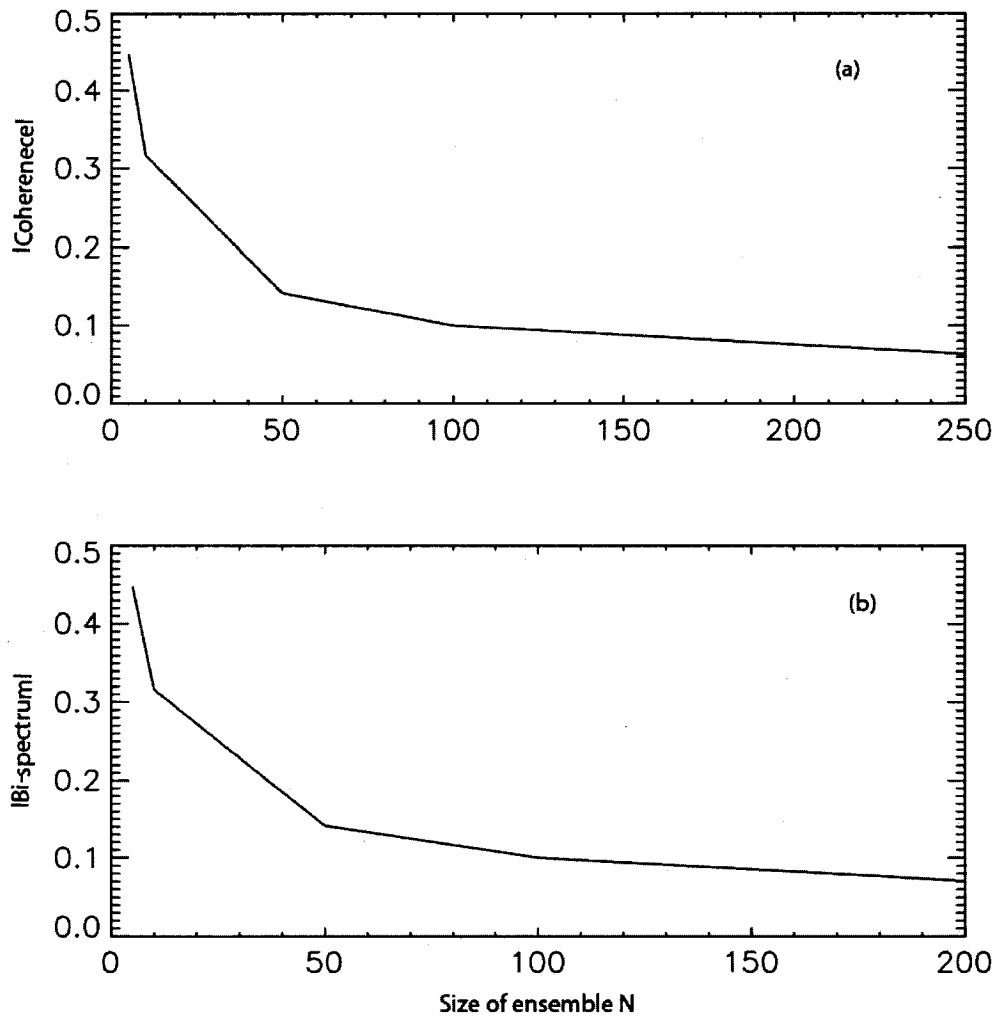
To completely characterize a fluctuation process requires that we have noiseless data and access to all possible realizations, which, from an experimental point of view, is not possible. We are faced with estimating certain features of the underlying fluctuation process of interest, based on a finite number of realizations. Fluctuation processes are characterized in part by their mean value, correlation function (coherence), and other higher order correlation functions (such as bi-coherence and quadro-coherence). For example, bi-coherence can be used to investigate the non-linearity between the fluctuation signals (fluctuation processes) which satisfy the sum rule. Every signal in the experiment includes some errors (randomness) due to limits in the experiment. We also have a limit in the size of the ensemble. These limits introduce uncertainties in our analysis. We use artificial data to look at the effect of noise and finite ensemble size on correlation functions of various orders. We also investigate the error in each correlation function analytically. We add various magnitudes of randomness to these data. We investigate the relation between the size of randomness added in the data and the critical number at each correlation function. The critical number is the size of ensemble where the correlation function with fully randomized data intersects the asymptotic (analytical) value of the correlation function with infinite number of realization.

### **Values of correlation functions with fully randomized signals**

Any order correlation functions with fully randomized signals give the same result :  $(\text{correlation function})^2 \sim 1/N$  where  $N$  is the size of the ensemble or number of realizations.. This is shown in graphs ( a ) and ( b ). Graph ( a ) is the coherence between



two fully randomized signals, which have oscillating real and imaginary parts, each with amplitude one. Graph ( b ) is the bi-coherence from three fully randomized signals, which have oscillating real and imaginary parts, each with magnitude one.



(a)Coherence and (b)bi-spectrum magnitudes with fully randomized signals

This  $1/N$  dependence can be derived analytically. We think about the coherence function first.

$$\gamma^2 = \frac{\langle |XY^*|^2 \rangle}{\langle |X|^2 \rangle \langle |Y|^2 \rangle}$$

$$\langle \rangle = \frac{1}{N} \sum_{i=1}^N$$

$$\langle |XY^*|^2 \rangle = \frac{1}{N^2} \sum_{i,j=1}^N (X_i X_j^* Y_i^* Y_j) = \frac{1}{N^2} \left( \sum_{i=1}^N |X_i|^2 |Y_i|^2 + \sum_{i \neq j} X_i X_j^* Y_i^* Y_j \right)$$

$$\langle |X|^2 \rangle = \frac{1}{N} \sum_{i=1}^N |X_i|^2$$

$$\langle |Y|^2 \rangle = \frac{1}{N} \sum_{j=1}^N |Y_j|^2$$

Therefore,

$$\gamma^2 = \frac{\sum_{i=1}^N |X_i|^2 |Y_i|^2}{\sum_{i,j=1}^N |X_i|^2 |Y_j|^2} + \frac{\sum_{i \neq j} X_i X_j^* Y_i^* Y_j}{\sum_{i,j=1}^N |X_i|^2 |Y_j|^2}$$

$$X_j = x_j e^{i\phi_j}$$

$$Y_j = y_j e^{i\phi_j}$$

If the data is fully randomized, the first term is  $\frac{N}{N^2} = \frac{1}{N}$  because  $|X_i|^2 |Y_i|^2 = |Z_i|^2$ , where

$Z$  is fully randomized signal, and the second term tends to zero for fully randomized signals for large  $N$ . We can show this analytically. The same results can be obtained in the bi-coherence and the quadro-coherence because  $Y$  signal (fully randomized) can be replaced by the product of two or three fully random signals. We can prove that the second term is zero as follow.

$$S = \frac{\sum_{j \neq k}^N X_j X_k^* Y_j^* Y_k}{\sum_{j,k=1}^N |X_j|^2 |Y_k|^2} = \frac{\sum_{j \neq k=1}^N x_j x_k y_j y_k e^{i(\phi_j - \phi_k + \vartheta_k - \vartheta_j)}}{\sum_{j,k=1}^N x_j^2 y_k^2} = \frac{\sum_{j > k}^N 2x_j x_k y_j y_k \cos(\phi_j - \phi_k + \vartheta_k - \vartheta_j)}{\sum_{j,k=1}^N x_j^2 y_k^2}$$

$x, y, \phi, \vartheta$ ..are..random.

Therefore,

$$S = \frac{\sum_{j=1}^{(N^2-N)/2} 2z_j \cos(\Phi_j)}{\sum_{j,k=1}^N x_j^2 y_k^2} = \frac{\sum_{j=1}^{(N^2-N)/2} 2Z_j}{\sum_{j,k=1}^N x_j^2 y_k^2} = 0 \dots \text{for } \dots \text{large } N$$

here.. $z_j = x_j x_k y_j y_k$ ..and.. $\Phi_j = \phi_j - \phi_k + \vartheta_k - \vartheta_j$

Z is fully randomized signal because x, y,  $\vartheta$ , and  $\phi$  are all randomized. Here, j, and k are all dummy variables. In S, upper part is zero, because  $\langle Z \rangle = 0$  for fully randomized signal Z.

### **The asymptotic value of correlation functions with partially randomized signals**

We examine coherence( $\gamma$ ), bi-coherence(b), and quadro-coherence(Q) in partially randomized signals. They all go to their analytical values asymptotically, when the size of ensemble is bigger. The signals used are exponential functions with magnitude of one. For coherence, two  $\exp(i\phi)$  are used. For bi-coherence,  $\exp(i\phi)$ ,  $\exp(2i\phi)$ , and  $\exp(3i\phi)$  are used. For quadro-coherence,  $\exp(i\phi)$ ,  $\exp(2i\phi)$ ,  $\exp(3i\phi)$ , and  $\exp(6i\phi)$  are used. Here,  $\phi$  is the phase. If no random signal is added to the above signals, all correlation functions have the value one because above signals in each correlation function satisfy the

summing rule. When add the random signals of various magnitudes to the above signals in each correlation function the result is less than one. For example, we add random signal  $R(-0.2 < R < 0.2)$  to each exponential signal (magnitude=1) in each correlation function. This is in the graph ( c ).

In coherence, we add fully random signals  $R$  to real and imaginary part of test data.

$$X = \cos(\phi) + R + i(\sin(\phi) + R)$$

$$Y = \cos(\phi) + R + i(\sin(\phi) + R)$$

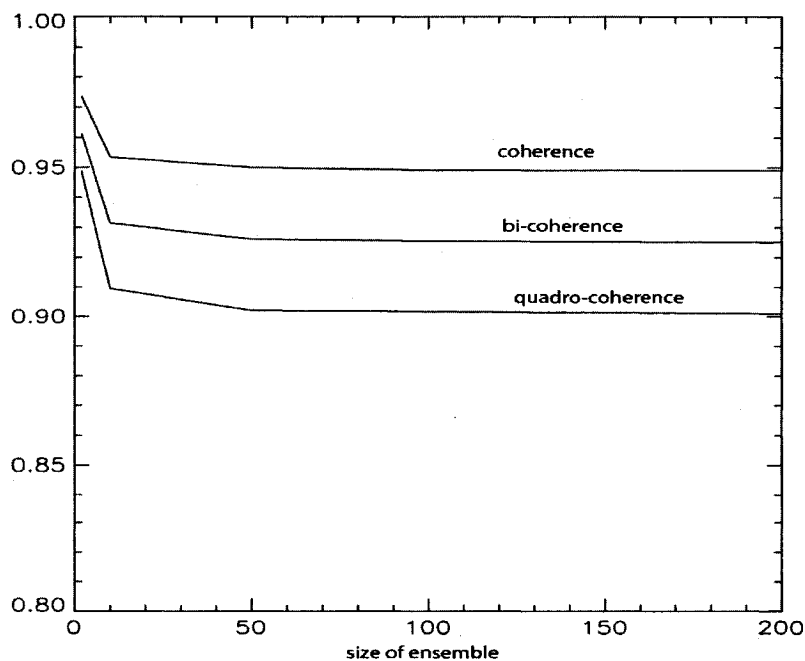
For bi-coherence,

$$X = \cos(\phi) + R + i(\sin(\phi) + R)$$

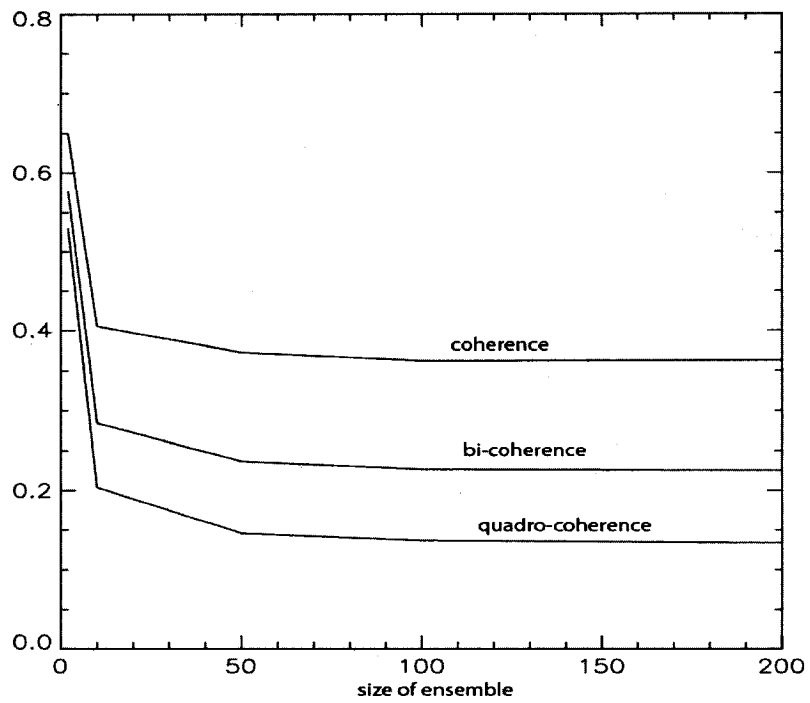
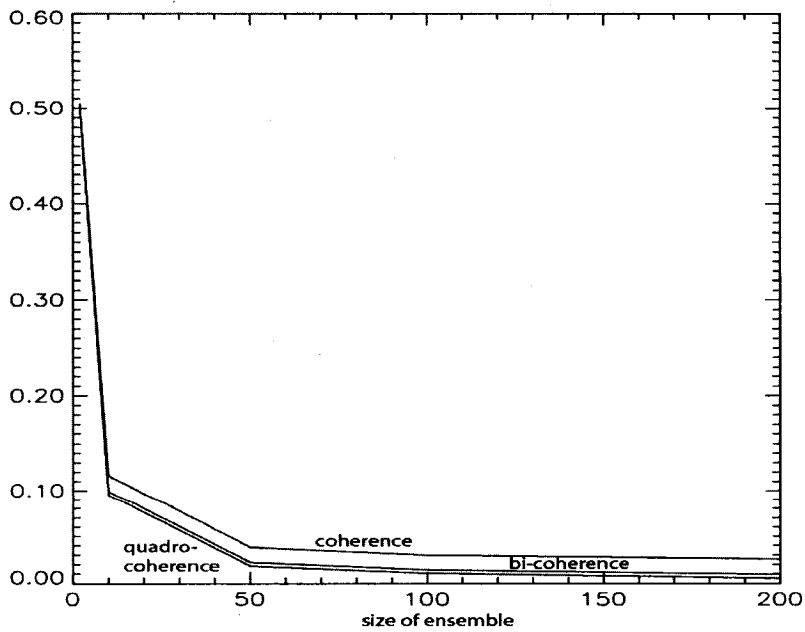
$$Y = \cos(2\phi) + R + i(\sin(2\phi) + R)$$

$$Z = \cos(3\phi) + R + i(\sin(3\phi) + R)$$

The graph ( d ) is when  $-1 < R < 1$ , in other words the magnitude of the random and non-random part are equal. The graph ( e ) is for  $-3 < R < 3$  in which case the randomized component is even larger fraction of the overall signal.



( c ) When the  $R$  is between  $-0.2$  and  $0.2$

(d) When the  $R$  is between  $-1$  and  $1$ (e) When the  $R$  is between  $-3$  and  $3$

**Analytical value of correlation function with partially random signals and the critical number**

We apply the analytical method to various orders of correlation functions. In this section, we find the asymptotic values of correlation functions for an ensemble of infinite size. We begin with the simple statistical review.

-What is the expectation value of the fully randomized signal?

$E[x]=0$  for any random signal  $x$ .

Here,  $E[x] = \int_{-a}^a P(x) \cdot x dx$  is the expectation value and  $P$  is the distribution function in

signal, where  $P(x)=1/2a$  because  $P$  should be constant in random signal and  $\int_{-a}^a P(x) dx = 1$ .

Here,  $a$  is the maximum value of signal in the above equation.

-What is the expectation value of the square of the fully randomized signal?

$$E(x^2) = \int_{-a}^a P(x) \cdot x^2 dx = \frac{1}{2a} \int_{-a}^a x^2 dx$$

here,  $P$  is the distribution function in random signal.

Therefore  $E[x^2] = \frac{a^2}{3}$  for any random signal  $x$  with the maximum  $a$ .

We start from coherence function.

$$\gamma^2 = \frac{\langle |X[l]Y[l]^*| \rangle^2}{\langle |X[l]|^2 \rangle \langle |Y[l]|^2 \rangle}$$

$$X[l = 1] = \cos(1t) + R + i \cdot (\sin(1t) + r)$$

$$Y[l = 1] = \cos(1t) + E + i \cdot (\sin(1t) + e)$$

for exponential signal with magnitude of 1.

We used the artificial sinusoidal signal because it is similar to real periodic experimental function. Every signal can be decomposed into sinusoidal functions by the Fourier transform if it is periodic or finite. We add random signals( $R$ ,  $E$ ,  $r$ , and  $e$ ) to the real and imaginary parts of the exponential function. Therefore, the exponential function becomes partially randomized.  $R$ ,  $E$ ,  $r$ , and  $e$  are all random signals with the same magnitudes.

Therefore,  $\langle E \rangle = \langle R \rangle = \langle e \rangle = \langle r \rangle = 0$ . Here,  $\langle \rangle$  means the expectation value coupled by averaging over an ensemble of realization of the signals. The important terms in computing  $\gamma^2$  are

$$\begin{aligned}\langle \cos t \rangle &= \cos t \dots \dots \langle \sin t \rangle = \sin t \\ \langle \cos^2 t \rangle &= \cos^2 t \dots \dots \dots \langle \sin^2 t \rangle = \sin^2 t \\ \langle E \cdot \cos t \rangle &= \cos t \langle E \rangle = 0 \\ \langle R \cdot E \rangle &= \langle R \cdot r \rangle = 0\end{aligned}$$

By the above equations, the coherence is as follow.

$$\begin{aligned}\gamma^2 &= \frac{1}{(1 + 2 \cdot \langle r^2 \rangle)^2} \\ \langle r^2 \rangle &= \frac{a^2}{3} \dots \dots \dots |r| \leq a \\ \therefore \gamma^2 &= \frac{1}{(1 + \frac{2a^2}{3})^2}\end{aligned}$$

-How about the others?

The bi-coherence is found using similar correlated sinusoidal functions with an additional random component.

$$b^2 = \frac{\left\langle \left| X[l_1 + l_2] X^*[l_1] X^*[l_2] \right|^2 \right\rangle}{\left\langle \left| X[l_1 + l_2] \right|^2 \right\rangle \left\langle \left| X[l_1] X[l_2] \right|^2 \right\rangle} = \frac{1}{(1 + 2 \cdot \langle r^2 \rangle)(1 + 8 \cdot \langle r^2 \rangle)}$$

$$X[l_1 = 1] = \cos t + R + i \cdot (\sin t + r)$$

$$X[l_2 = 2] = \cos 2t + E + i \cdot (\sin 2t + e)$$

$$X[l_1 + l_2 = 3] = \cos 3t + P + i \cdot (\sin 3t + p)$$

$$\langle r^2 \rangle = \frac{a^2}{3} \dots \dots \dots |r| \leq a$$

R, E, P, r, e, and p are all random with the same magnitudes.

The quadro-coherence is found as follow.

$$Q^2 = \frac{\left\langle \left| X[l_1 + l_2 + l_3] X^*[l_1] X^*[l_2] X^*[l_3] \right|^2 \right\rangle}{\left\langle \left| X[l_1 + l_2 + l_3] \right|^2 \right\rangle \left\langle \left| X[l_1] X[l_2] X[l_3] \right|^2 \right\rangle} = \frac{1}{(1 + 2 \cdot \langle r^2 \rangle)(1 + 26 \cdot \langle r^2 \rangle)}$$

$$X[l_1 = 1] = \cos t + R + i \cdot (\sin t + r)$$

$$X[l_2 = 2] = \cos 2t + E + i \cdot (\sin 2t + e)$$

$$X[l_3 = 3] = \cos 3t + P + i \cdot (\sin 3t + p)$$

$$X[l_1 + l_2 + l_3 = 6] = \cos 6t + K + i \cdot (\sin 6t + k)$$

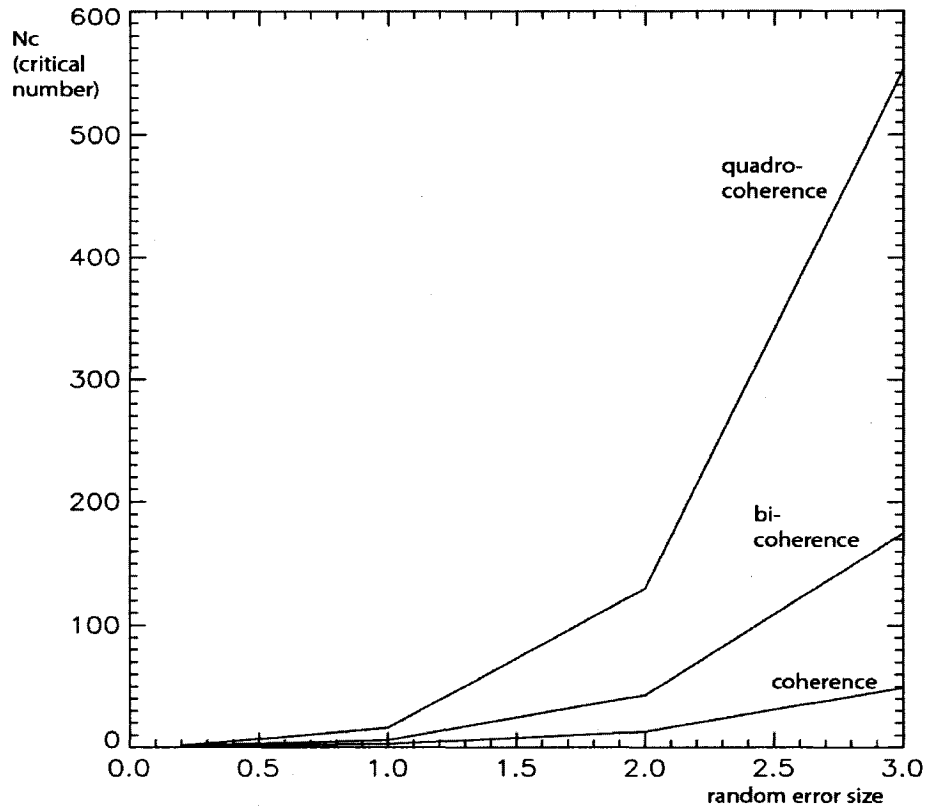
R, E, P, K, r, e, p, and k are all random with the same magnitudes.

$$\langle r^2 \rangle = \frac{a^2}{3} \dots \dots \dots |r| \leq a$$

The critical number is the size of ensemble when the analytical value (when ensemble size is infinite) of correlation function with partially randomized signals (  $R < 0.2$ ,  $R < 1$ , and  $R < 3$  in our case) matches the value of correlation function with fully randomized signal ( $\sim 1/N$  in section 1). Therefore critical number is inverse of analytical value or



1/(analytical value). We test the critical values of each correlation functions (coherence, bi-coherence, and quadro-coherence) with different values of partially random signals. We add three different random signals to our exponential functions in each correlation function. These can be seen in graph ( f ).



( f ) critical value vs magnitudes of added randomized signal in each correlation function

If we add bigger error to correlation function, the critical value of correlation function is increased. The higher order correlation function has bigger critical value for the same size of error.